Journal of Materials Research and Technology 41 (2026) 1463–1478

Contents lists available at ScienceDirect

Journal of Materials Research and Technology

journal homepage: www.elsevier.com/locate/jmrt

The effect of aging precipitation on the fretting wear behavior of 17-4 PH stainless steel used for tight fit assemblies

Xiaojun Xu [a,b,*], Binbin Gan [a], Ting Yang [a], Xiaoqin Zha [b,**], Jianjun Long [a,c], Xiaoyu Zhang [d], Pingyang He [a], Hao Li [a], Minhao Zhu [a]

[a] Key Laboratory of Advanced Technologies of Materials (Ministry of Education), School of Materials Science and Engineering, Southwest Jiaotong University, Chengdu, 610031, China
[b] National Key Laboratory of Marine Corrosion and Protection, Luoyang Ship Material Research Institute, Luoyang, 471023, China
[c] Institute for Applied Materials (IAM), Karlsruhe Institute of Technology (KIT), Kaiserstrasse 12, Karlsruhe, 76131, Germany
[d] School of Mechanical Engineering, Southwest Jiaotong University, Chengdu, 610031, China

ARTICLE INFO

Keywords:
17-4 PH stainless steel
Fretting wear
Cu-rich precipitate
Failure mechanisms

ABSTRACT

An experimental study on fretting wear behavior of a 17-4 PH stainless steel aging heat treated to different microstructural features with different precipitate variants is presented. The fretting wear tests with respect to different fretting running regimes were carried out. The microstructural observations show that below 460 °C of aging temperature, only NbC precipitates were observed. While as the aging temperature reached the 460 °C, not only NbC but also Cu-rich precipitates (CRPs) can be found, and even more so at higher aging temperature. Wear results indicate that in the partial slip regime (PSR) and mixed fretting regime (MFR), the fretting wear volume decreases with the aging temperature increases up to 410 °C, beyond which the wear volume commences to arise. The sample T2 (410 °C) has a highest fretting wear resistance. In contrast, in gross slip regime (GSR), although the correlation of fretting wear volume and aging temperature shows a similar trend with that in PSR and MFR, the sample T3 (460 °C) has a highest fretting wear resistance in GSR. It suggests that the precipitates have significant effect on fretting wear resistance, and their effects are fretting running regime dependent. Subsurface observations demonstrate that fine-size CRPs could promote the formation of the compacted and oxide-contained plastic deformation layer, which can improve the fretting wear resistance. The results can provide a good guideline to optimize the target microstructure for a specific working condition or tune the working condition parameter to allow a best fretting wear resistance.

1. Introduction

Precipitation-hardening (PH) stainless steels combining the good balance of strength and ductility, good corrosion resistance and formability as well as manufacture facilitation, have been widely used for tight fit assemblies in industrial applications [1,2], such as aerospace [3,4], navigation engineering [5,6], nuclear power plants [7,8]. The promising mechanical properties are due to the composite nature of the hard constituent (martensitic substrate) and a little soft phase (ferrite) along with the precipitation strengthening effect. So far, a lot of work has been done to study the tensile properties and other mechanical properties of PH stainless steels as functions of many variables, such as aging temperature [9,10], retained austenite [11,12], precipitates [9,13,14]. However, as the key components of tight fit assemblies, the PH stainless steels are often suffered from the fretting damage, which always happens as contacting steels are experienced oscillatory movement of small amplitude. This can lead to the premature catastrophic failures of materials, i.e., the removal of surface materials and/or the development of cracks [15–17]. It has increasingly become a significant problem for tight fit assemblies, which can reduce the running safety and life-time [18–23]. There have been many studies on the fretting damage of PH stainless steels, but mostly limit to the fretting fatigue damage aiming to understand the behavior of fatigue crack so as to allow a best fatigue performance [24,25]. For instance, Peng et al. [3]studied the

---

* Corresponding author. Key Laboratory of Advanced Technologies of Materials (Ministry of Education), School of Materials Science and Engineering, Southwest Jiaotong University, Chengdu, 610031, China
** Corresponding author.
E-mail addresses: xiaojunxu@swjtu.edu.cn (X. Xu), zha1687827905@163.com (X. Zha).

https://doi.org/10.1016/j.jmrt.2026.01.039
Received 2 September 2025; Received in revised form 15 December 2025; Accepted 6 January 2026

fretting fatigue behavior of 15-5 PH stainless steel with different bending fatigue loads, which showed that the concentration of residual stress is prone to be formed in the mixed fretting regime, consequently promoting the initiation and propagation of cracks and hence aggravating the damage in mixed fretting regime. Pape et al. [26,27] commented that the PH 13-8 Mo stainless steels experienced significant reductions in fatigue strength due to fretting, and also pointed out that the susceptibility to fretting fatigue is quite high in mixed fretting regime. Moreover, Liu et al. [28]reported the fretting fatigue of the 17-4 PH stainless steel with gradient structure, which demonstrated that nano-grain growth and dislocation density reduction can enhance crack initiation resistance. In general, fretting fatigue is a failure damage mode, which is often caused by an external cyclic load acting on surfaces upon fretting contact [29]. It always leads to the initiation and propagation of cracks, consequently resulting in a reduction of fatigue life. In contrast, fretting wear is primarily a surface degradation process caused by small-amplitude oscillatory slip between two contacting surfaces, which often leads to the removal of materials from the surfaces due to small and repetitive movements. It primarily causes the formation of wear debris and surface damage, such as ploughing, delamination, and cracks. Hence, the dominate damage mechanism could be completely different between fretting wear and fretting fatigue. Nevertheless, the fretting wear of PH stainless steel corresponding to the material removal behavior has been studied less. The study on fretting wear will provide a new insight into reveal the surface damage of 17-4 PH stainless steels in a real-life service situation. In addition, although the surface modification has also been considered as an effective method to enhance the surface wear resistance of PH stainless steels, such as plasma nitrocarburizing [30], plasma nitriding [31–35], shot peening [36–38], and ultrasonic surface rolling [28], they mainly concentrate on the sliding wear and/or corrosion. In contrast, systematic investigations into the effect of the microstructural features on the fretting wear for PH stainless steels are still lacking. The response of different precipitates in 17-4 PH steels on fretting wear under different fretting run regimes is still not yet clear.

Moreover, for PH stainless steels the precipitation strengthening by aging treatments is the critical parameter to enhance the mechanical properties [9,39,40]. During the aging process [13,41–43],the Cu-rich precipitates (CRPs) and the other precipitations were formed depending on the aging temperature, which are capable of blocking the dislocation effectively by shearing mechanism and/or Orowan bypass mechanism, as a result significantly improving the strength of a material. In particular to the CRPs, it can play a much important role in determining the mechanical properties for PH stainless steels compared to the other precipitates [41,44]. As studied in Refs. [45–51], with increasing the aging temperature and/or the time, the nano-CRPs has a series of microstructural evolutions from BCC→9 R→FCC(ε-Cu), while the CRPs become coarse and can be transformed from sphericity to cylindricity along dislocations or grain boundaries after long-term aging treatment. As a result, it can reduce the strengthening effect and hence lower the material strength depending on the aging temperature and time [13,52]. These studies clearly demonstrate that the precipitations have significant influence on the mechanical properties, which certainly affect the fretting wear. However, the response of precipitation in PH stainless steels on fretting wear under different fretting regimes has been not studied yet.

In the present work, a 17-4 PH steel was selected for this study, which is due to the fact that the 17-4 PH steel represents one of very successful engineering PH steel family, and has been widely used as tight fit assemblies, such as rivets, bolts, and dovetail joint, in the aerospace, navigation engineering and nuclear power plants. Series of aging heat treatments with different aging temperature for a 17-4 PH stainless steel were conducted to obtain different microstructural features with variant precipitates. The fretting wear behavior of resulting microstructures with different well-characterized precipitates was evaluated by using fretting wear test rig designed under different fretting running regimes. The morphology of the resulting worn scars and the development of plastic deformation layer due to fretting wear were observed to reveal the fretting wear resistance and failure mechanisms. The effect of precipitates on the fretting wear resistance was discussed. The study will provide a guideline to optimize a proper microstructure of 17-4 PH stainless steels for a given application or tune the application conditions to allow a best fretting wear performance of a given 17-4 PH stainless steels.

2. Experiments

2.1. Aging heat treatment conditions

The as-received 17-4 PH stainless steel was chosen for this study. Its chemical composition was determined by a spark emission spectrometer (QSN750, OBLF), as seen in Table 1. The resulting microstructure was given in Fig. 1, which is consisted of martensite substrate and δ-Fe phase. The steel plates were cut from the as-received steel bar with the size of 100mm × 50mm × 3 mm, and was then solid solution treated at 1040 °C for 1 h followed by water quenching with the use of a muffle furnace (SG-XQL-1400, SIOM) with an argon atmosphere protection. The heating rate was 20 °C/min. The accuracy of temperature control on the sample is measured to be within ±5 °C. After solid solution treatment, the subsequent aging treatments were performed at 360 °C, 410 °C, 460 °C,510 °C, 620 °C for 4 h followed by oil cooling, respectively. Here it should be mentioned that the selection of oil cooling is intended to decrease the content of retained (reversed) austenite and meanwhile lower the residual stress in the final microstructure state.

It is known that there could be reversed austenite formed during aging process via austenite reverse transformation [53–55]. As stated in Refs. [56–58], the amount of reversed austenite decreases with increasing the cooling rate at the same aging temperature, which is due to the fact that a higher thermal stress and higher concentration of vacancies from higher cooling rate make the reversed austenite more unstable. As a result, the unstable reversed austenite can be re-transformed to new martensite during the cooling process at higher cooling rate, consequently decreasing the content of the retained (reversed) austenite. The schematic drawing of heat treatment routes was shown in Fig. 2, and the heat treatment parameters are summarized in Table 2.

2.2. Hardness measurements and tensile tests

The micro-hardness of samples was determined by a Vickers indenter (HVS-1000Z, JOHOYD) under a normal load of 2 N, and ten measurements were done to report an average. The tensile tests for each aging treatment sample were executed three times with the tensile tester produced by LISHI (Shanghai) Instrument (LF5504). Each test specimen is flat shape with a gauge length of 25 mm following the ASTM-E8 standard. The strain rate is 10^{-3}/s.

2.3. Fretting wear experiments

In the present study, a high precision fretting wear test rig as reported in Ref. [59] was utilized to conduct the fretting wear test at room temperature with a relative humidity ranging from 50 % to 60 %. A ball-on-plate contact configuration was chosen, and a GCr15 ball with a diameter of 10 mm was employed as the counter body. The sample placed on the table was derived by a piezoelectric ceramic actuator, aiming to realize the tangential reciprocation with a range from 0 to 180

Table 1
The chemical composition (wt.%) of the 17-4 PH stainless steel.

Elements composition (in wt.%)								
Elements	Cr	Cu	Ni	Nb	Si	Mn	C	Fe
17-4 PH	15.62	3.30	3.82	0.30	0.37	0.35	0.03	Bal.

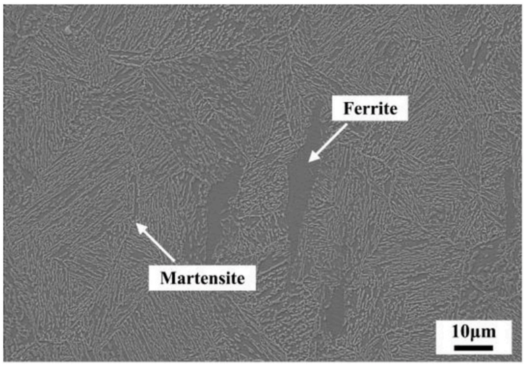

Fig. 1. SEM image of the microstructure of the as-received 17-4 PH stainless steel.

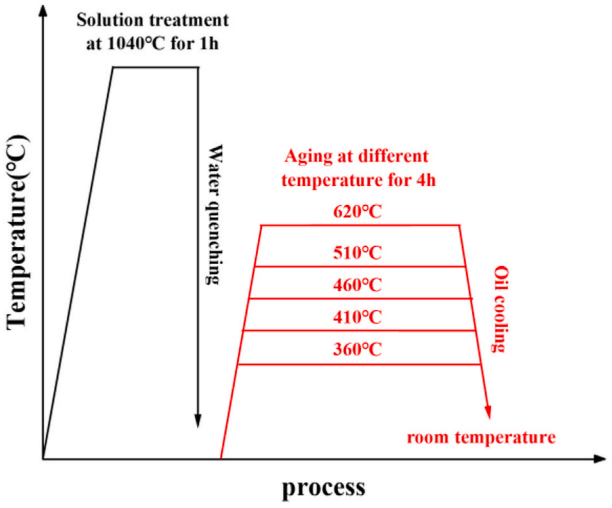

Fig. 2. Schematic illustration of heat treatment routes.

Table 2
Heat treatment conditions.

Heat treatment cycles	
Solid solution	Aging temperature & time
T1: 1040 °C, 1 h	360 °C, 4 h
T2: 1040 °C, 1 h	410 °C, 4 h
T3: 1040 °C, 1 h	460 °C, 4 h
T4: 1040 °C, 1 h	510 °C, 4 h
T5: 1040 °C, 1 h	620 °C, 4 h

μm. Meanwhile, a capacitive displacement sensor of high precision was used to measure the displacement and give the real-time feedback to actuator, so as to control the displacement. The normal load applied on the sample was imposed by a compressed spring, which was measured by a stress sensor. Moreover, a piezoelectric force sensor was placed between the sample table and the base to acquire the friction force during all fretting wear process. Prior to fretting wear test, all samples (15mm × 10mm × 3 mm) were mechanically polished following a standard metallographic preparation with a final surface roughness Ra of about 0.1 μm. During the fretting wear test, the instantaneous displacement (*D*) and friction force (F_t) were monitored and recorded per cycle, presenting a live plot of the fretting loop F_t-*D*. The instantaneous displacement (*D*) is referring to the movement of fretting running at a particular instant in time. Each test was repeated 3 times to ascertain the reproducibility of the results reported. The fretting frequency is 5 Hz, and the displacement amplitude is 1 μm, 5 μm, 10 μm, 20 μm, 60 μm, respectively. The cyclic numbers is 3×10^4. The detailed test parameters of fretting wear test are list in Table 3.

2.4. *Metallography and worn scar observations*

Each tested sample for metallurgical characterization was polished following standard metallographic preparation, i.e., the sample was firstly mechanically grounded with SiC abrasive papers of 180#, 400#, 800#, 1500# and 2000#, and afterward was polishing by the diamond suspensions with diameter 2.5 μm, and finally was etched with an etching solution composed of 5 g $FeCl_3$, 15 ml HCl and 75 ml distilled water. A scanning electron microscope (SEM, Sigma 300, ZEISS) at a voltage of 3 kV and transmission electron microscope (TEM, Tecnai G2 F20, FEI) were used for the microstructural examinations. The elemental analysis of the precipitates were conducted by the TEM-energy dispersive spectrometer (EDS, XFlash, Bruker). The specimen for TEM analysis was firstly grounded by 2000# SiC abrasive paper to a thin sheet with a thickness of 80 μm, and then was punched into a small disc with a diameter of 3 mm. Afterward, the disc was twin-jet electropolished at −25 °C using an electrolyte consisting of 90 % ethanol and 10 % perchloric acid (Struers TenuPol-5) to perforation for TEM observations. The X-ray diffraction (XRD, Ultima IV, Rigaku) with Cu Kα radiation source at a voltage 40 kV and a current of 40 mA was used to determine the microstructural phase of all heat-treated samples. The 2θ was ranged over 10–120° with a step of 0.02° and a counting time of 1s/step. The wear loss and the profile of worn scars were examined by a 3D-white-light interferometer (GTK-16–0295, Bruker). The tribo-oxidation on subsurface was probed by the SEM-EDS (Xplore 30, Oxford). The acquisition time for each EDS line scan was kept consistent at approximately 10 min. After each fretting wear test, the surface morphologies of the worn scars and the resulting cross section were observed by SEM at 5 kV.

3. Results

3.1. *Observations of microstructures and aging precipitation*

The microstructures produced by different heat treatments (as shown in Table 2) are presented in Fig. 3. As can be seen, samples T1 to T5 subjected to aging treatment following solid solution mainly possess a microstructure consisting of δ-ferrite and lath martensite as indicated in Fig. 3. After solid solution, the martensite formed is oversaturated, and the formation of δ-ferrite was due to the high content of ferrite forming alloy elements such as Cr element, as stated in Ref. [60]. Upon the subsequent aging treatment, as reported in Refs. [61–63], the reduction of residual stress and dislocation in the oversaturated martensite took place, which is attributed to the fact that the high temperature can offer high driving force for atomic diffusion and dislocation motion. It can prompt the atoms to transit from the non-equilibrium state to equilibrium state, and then decrease the degree of lattice distortion, consequently reducing the residual stress. Meanwhile, the martensitic lath becomes coarse with the increase of aging temperature as stated in Ref. [64], along with the precipitation formation. In addition, Fig. 4 presents the XRD results of all aged samples. With the exception of the T5 (620 °C) sample, no visible peak of γ phase can be found for all other samples. For the microstructure of T5 sample, there is a very week peak

Table 3
The parameters of fretting test.

Test parameters	
Normal load	60 N
Displacement amplitude	1 μm, 5 μm, 10 μm, 20 μm, 60 μm
Frequency	5 Hz
Cyclic numbers	3×10^4
Relatively humidity	50 %–60 %

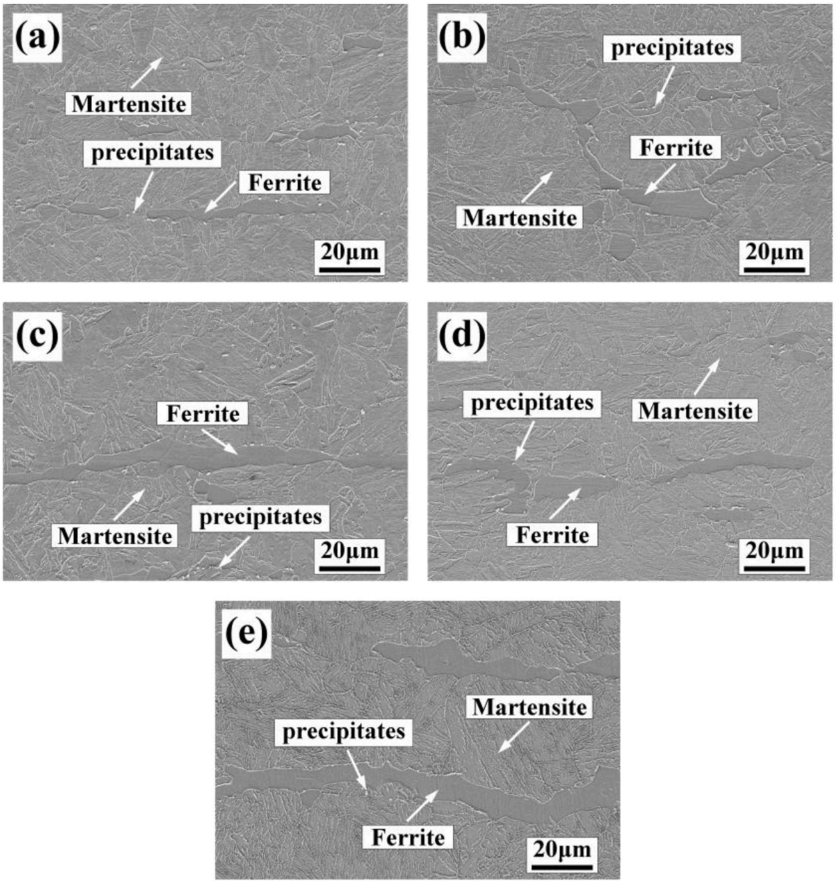

Fig. 3. SEM images of 17-4 PH stainless steel with different aging temperature: (a)360 °C; (b); 410 °C (c); 460 °C; (d)510 °C; (e) 620 °C.

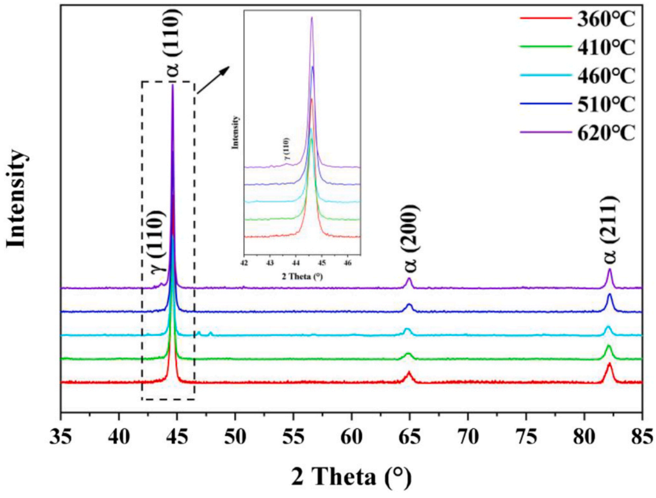

Fig. 4. XRD spectrums of all aged 17-4 PH stainless steels.

of γ (FCC) phase, which is nearly comparable to the background noise. It can be therefore inferred that there is reverted austenite formed during the aging process at the highest aging temperature of 620 °C, but the amount of reverted austenite is tiny. The XRD result is further consistent with the intention of selecting the oil cooling to decrease the content of retained (reversed) austenite in final microstructure. Of importance is the formation of the precipitates during aging process (as seen in Fig. 3), which can play an important role in determining the mechanical properties [50,51,65,66], including the fretting wear resistance. Hence, the TEM was utilized to further identify the precipitates and probe their structures. Fig. 5 gives the resulting TEM images of samples (T1-T5 samples) subjected to different aging temperature. As can be seen in Fig. 5(a), the T1 sample (360 °C) presents a typical lath martensitic microstructure with a high density of dislocation, accompanied by evident nano-precipitates (as seen in Fig. 5(b)). With increasing the aging temperature up to 410 °C, 460 °C, 510 °C, 620 °C, it seems that the width of martensitic laths gets larger as seen in Fig. 5(c–e), especially at the higher aging temperature where the lath boundary becomes unclear as shown in Fig. 5(g–j). Meanwhile, the dislocation density reduced due to the dislocation recovery upon aging, as seen in Fig. 5(c, e, g, j), which is consistent with the statement above. Moreover, the nano-precipitates can be clearly observed in bright field TEM images, as indicated by the yellow arrows in Fig. 5(d, f, h). Combined with the selected area electron diffraction (SAED) patterns (seen in Fig. 5(i)), as the aging temperature is below and at 510 °C, the precipitates were identified as NbC. When the aging temperature increases to 620 °C, on the basis of the TEM-EDS results (Fig. 5(m) and (n)) and SAED patterns (Fig. 5(o) and (p)), not only the spherical NbC precipitates but also the short rod-like ε-Cu (i.e., CRPs) as well as G phase precipitates can be found, as marked by yellow and red arrow in Fig. 5(k and l), respectively. In addition, the precipitates coarsening took place with the increase of aging temperature. It should be pointed out the copper-rich precipitates (CRPs) have different variants and can evolve from BCC→9 R→FCC(ε-Cu) with the aging temperature increase [13,45,46,48,49]. It implies that at the highest aging temperature of 620 °C, the CRPs have approached the final state corresponding to the ε-Cu precipitates. Accordingly, it can be deduced that there could be other CRPs variants formed below 620 °C, despite the fact that no CRPs was found in the current microstructural investigation due to the characterization limitation for the finer size CRPs. Hence, a high-resolution TEM will be utilized to further probe the CRPs next.

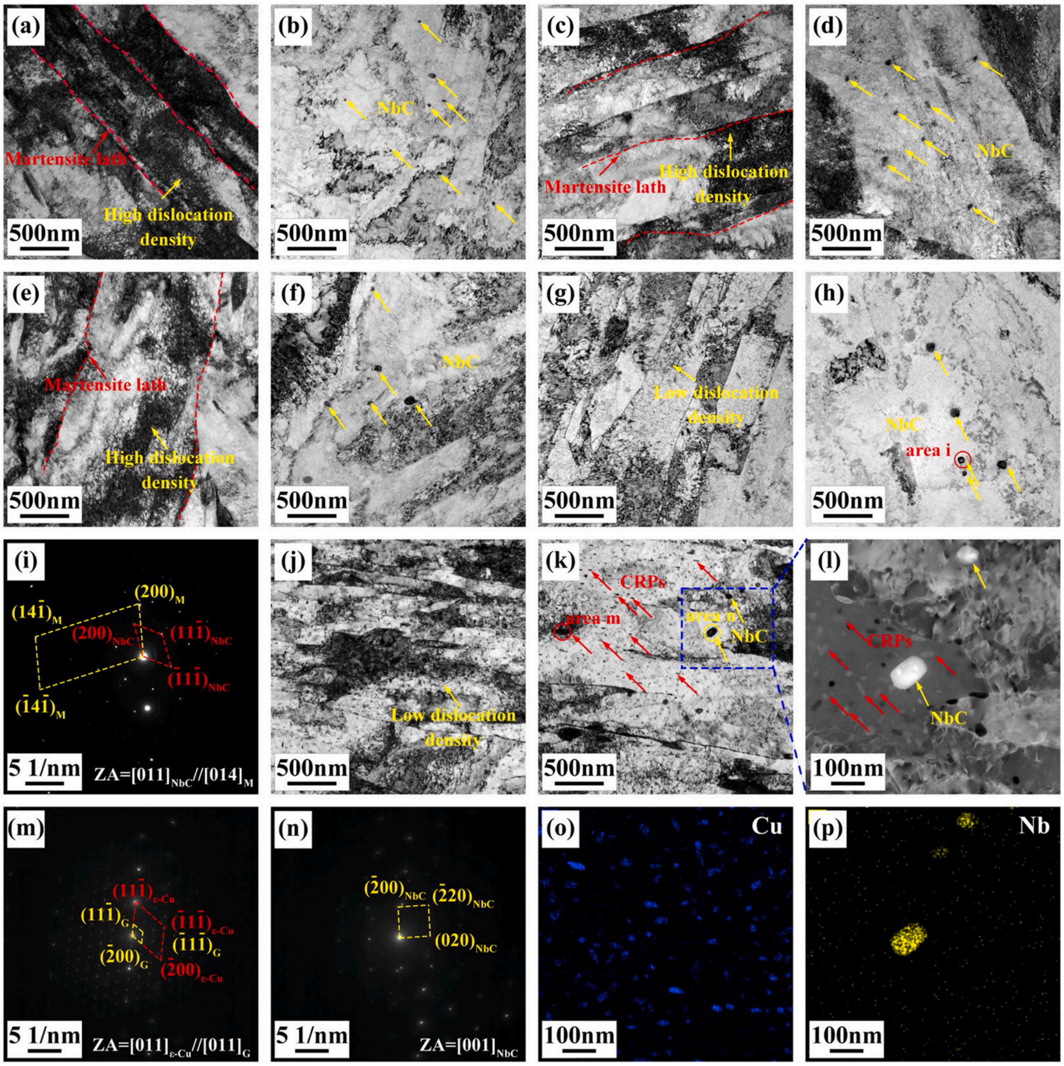

Fig. 5. Bright field TEM images and SAED patterns of the samples for different aging temperature: (a, b) 360 °C; (c, d) 410 °C; (e, f) 460 °C; (g, h, i) 510 °C; (j, k, l, m, n) 620 °C, and the EDS results of the sample 620 °C: (o) Cu element, (p) Nb element. Note: Fig. 5(i) is the SAED pattern referring to the position i as marked in Fig. 5(h); Fig. 5(l) is the high angle annular dark filed (HAADF) image of the blue rectangle area as marked in Fig. 5(k); Fig. 5(m, n) are the SAED patterns of the red and yellow circular area as marked in (k), respectively; Fig. 5(o, p) are the EDS results referring to Fig. 5(l).

3.2. Copper-rich precipitates (CRPs)

In order to further reveal the CRPs variants below 620 °C, a high-resolution TEM images acquired with beam reflection $[111]_{\alpha\text{-Fe}}$, fast Fourier transform (FFT) patterns and inverse fast Fourier transform (IFFT) images are gives in Figs. (6-7), respectively. It should be mentioned that there is indeed no evident CRPs found at 360 °C and 410 °C, hence no resulting HAADF and high-resolution transmission microscopy (HRTEM) images were given here. While with the increase of aging temperature up to 460 °C, lots of CRPs can be clearly observed in Fig. 6(a, b). Based on the HRTEM images and FFT patterns as seen in Fig. 6(d–f), the CRPs are dominant BCC and 9 R phase. As reported in Ref. [67], if the size of CRPs is smaller than 6 nm (i.e., the critical transformation size of BCC structure transformed to 9 R structure), CRPs are generally considered to be BCC structure. According to the results in Fig. 6(a, b) where the size of CRPs is roughly smaller than 6 nm, it suggests that the CRPs are dominant BCC phase along with some 9 R phase. The EDS mapping of Nb element in Fig. 6(b) refers to the distribution of Nb dissolved in the matrix. Moreover, the FFT pattern displayed in Fig. 6(d) illustrates that the orientation relationship between the 9 R-CRPs and martensite matrix obeyed the rule that $[110]_{9R\text{-CRPs}}//[111]_{BCC\text{-M}}$, $(11\bar{4})_{9R\text{-CRPs}}//(01\bar{1})_{BCC\text{-M}}$, as stated in Refs. [13,50,51,68]. In addition, for the Cu-rich precipitate of 9 R structure, it further demonstrates that the atom arrangement along $[001]_{9R}$ is ABC|BCA|CAB, showing a monoclinic system, as presented in the IFFT image of Fig. 6(e).

As the aging temperature increases to 510 °C, it is clear that lots of CRPs can also be found, while the Cu-rich precipitates became coarser and reached over 10 nm, as seen in Fig. 7(a). Due to the higher aging temperature, therefore, the CRPs were evolved to dominant 9 R structure, as shown in Fig. 7(d–f). Moreover, it should be mentioned that the black spots in Fig. 7(a) were also corresponding to the Cu-rich precipitates, which is the result of CRPs falling off during the preparation of TEM samples as pointed out in Ref. [41]. In addition, Fig. 7(e) also demonstrates that the 9 R structure is still a monoclinic system, which is same as shown in Fig. 6(e) (460 °C).

3.3. Hardness and tensile test results

Fig. 8 shows the micro-hardness (Hv), yield strength (YS), the ultimate tensile strength (UTS) and the total elongation (TE) as a function of the aging temperature for all conditions. It can be seen that, the trend of increasing Hv, YS and UTS with increasing aging temperature continues up to a critical aging temperature beyond which the Hv, YS and UTS

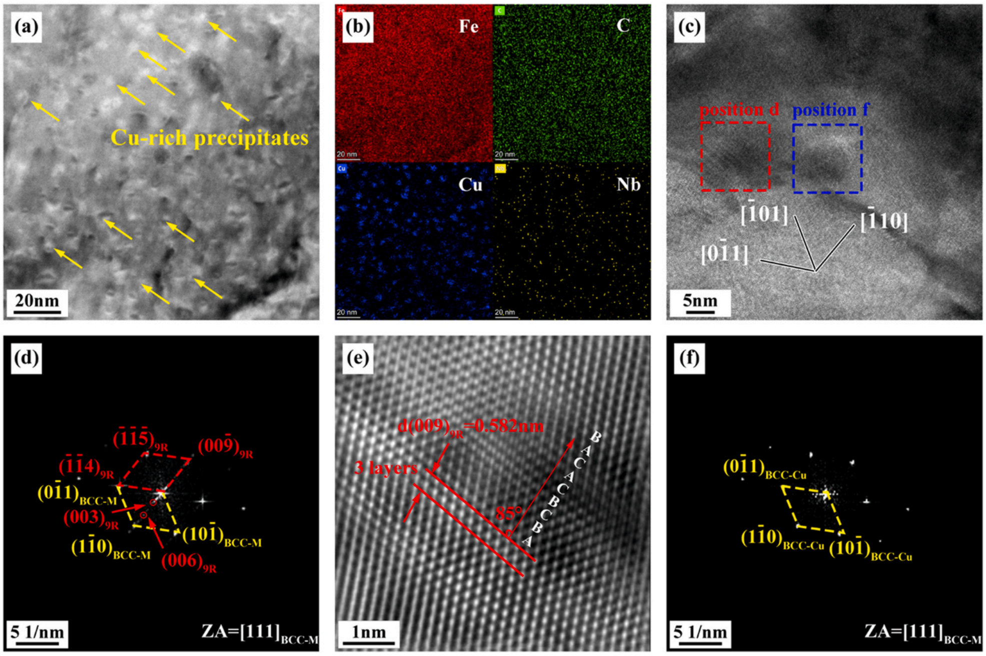

Fig. 6. HAADF image and HRTEM images of the sample with aging temperature of 460 °C: (a) HAADF image of CRPs; (b) EDS results; (c) HRTEM image of CRPs; (d; e) FFT pattern and IFFT image referring to the position d; (f) FFT pattern referring to the position f.

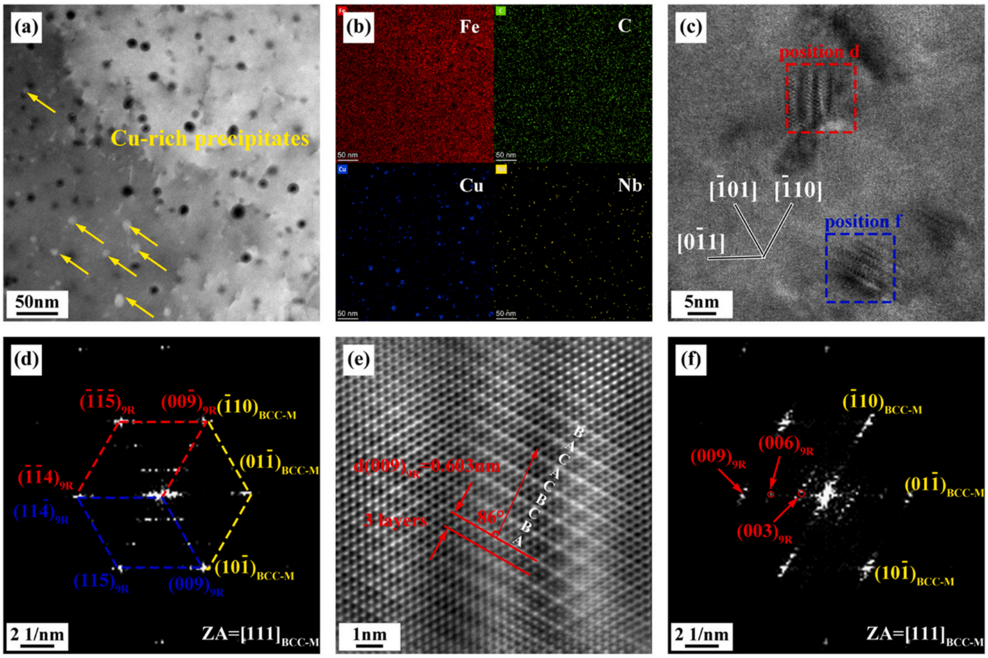

Fig. 7. HAADF image and HRTEM images of the sample with aging temperature of 510 °C: (a) HAADF image of CRPs; (b) EDS results; (c) HRTEM image of CRPs; (d; e) FFT pattern and IFFT image referring to the position d; (f) FFT pattern referring to the position f.

starts to decrease again. While the TE shows an opposite trend. The sample T3 (460 °C) possesses the maximum YS and UTS, but the maximum Hv for the sample T2 (410 °C). The increases in Hv, YS and UTS are the main result of precipitation strengthening due to the formation of precipitates (CRPs, NbC) upon aging. While the decrease in Hv, YS and UTS could be related to the fact that the further increase in aging temperature leads to the reduction of dislocation, precipitates coarsening, as well as martensitic lath widening, consequently resulting in strength decrement.

3.4. *The determination of fretting run regimes*

The fretting hysteresis loops consisted of the varied friction force (F_t) versus the instantaneous displacement (D) as a function of cyclic number (F_t-D-N curves) under the applied normal load of 60 N for all samples are given in Fig. 9. According to the variation of the F_t-D-N curves, three different fretting running regimes [69], i.e. partial slip regime (PSR), mixed fretting regime (MFR) and gross slip regime (GSR), can be observed. In general, fretting running regimes are used to describe the degree of relative slip at contact interface between two surfaces

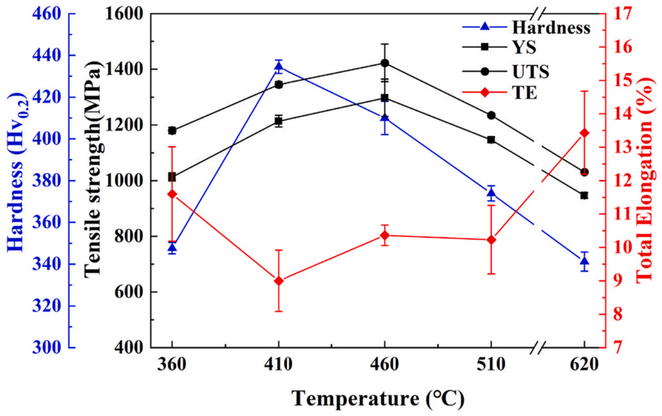

Fig. 8. The yield strength, ultimate tensile strength, total elongation and Vicker's hardness as a function of the aging temperature.

undergoing fretting wear, which strongly depends on the displacement and load conditions [69–72]. Each regime has different wear responses with respect to fretting wear resistance and wear mechanisms. At a small displacement amplitude less than 5 μm, the F_t-D curve of each sample presents a shape of a nearly line as shown in Fig. 9(a, d, g, j, m). It indicates that the fretting wear process had run in the PSR under these conditions. With increasing to a higher displacement ($D \geq 60$ μm), as seen in Fig. 9(c, f, i, l, o), the F_t-D curves are all open and show quasi-rectangular shape for all test cycles, which indicate that a gross slip took place during the whole fretting wear process, referring to GSR. For an intermediate displacement amplitude such as 20 μm, the F_t-D curves are composed of quasi-rectangular loop at the run-in stage and elliptical loops at the steady stage, as seen in Fig. 9(b, e, h, k, n). As reported in Zhou's work [69], at the run-in stage, given the fact that there are some oxidation films, pollution and adsorbates on the original surface of sample, it can promote the relative slip, consequently presenting a rectangular shape as displayed at the low cyclic numbers. Subsequently, with the removal of the oxidation films, pollution and adsorbates due to the fretting wear, the fresh surface of a material will directly contact with the counter-body, which can increase the adhesive

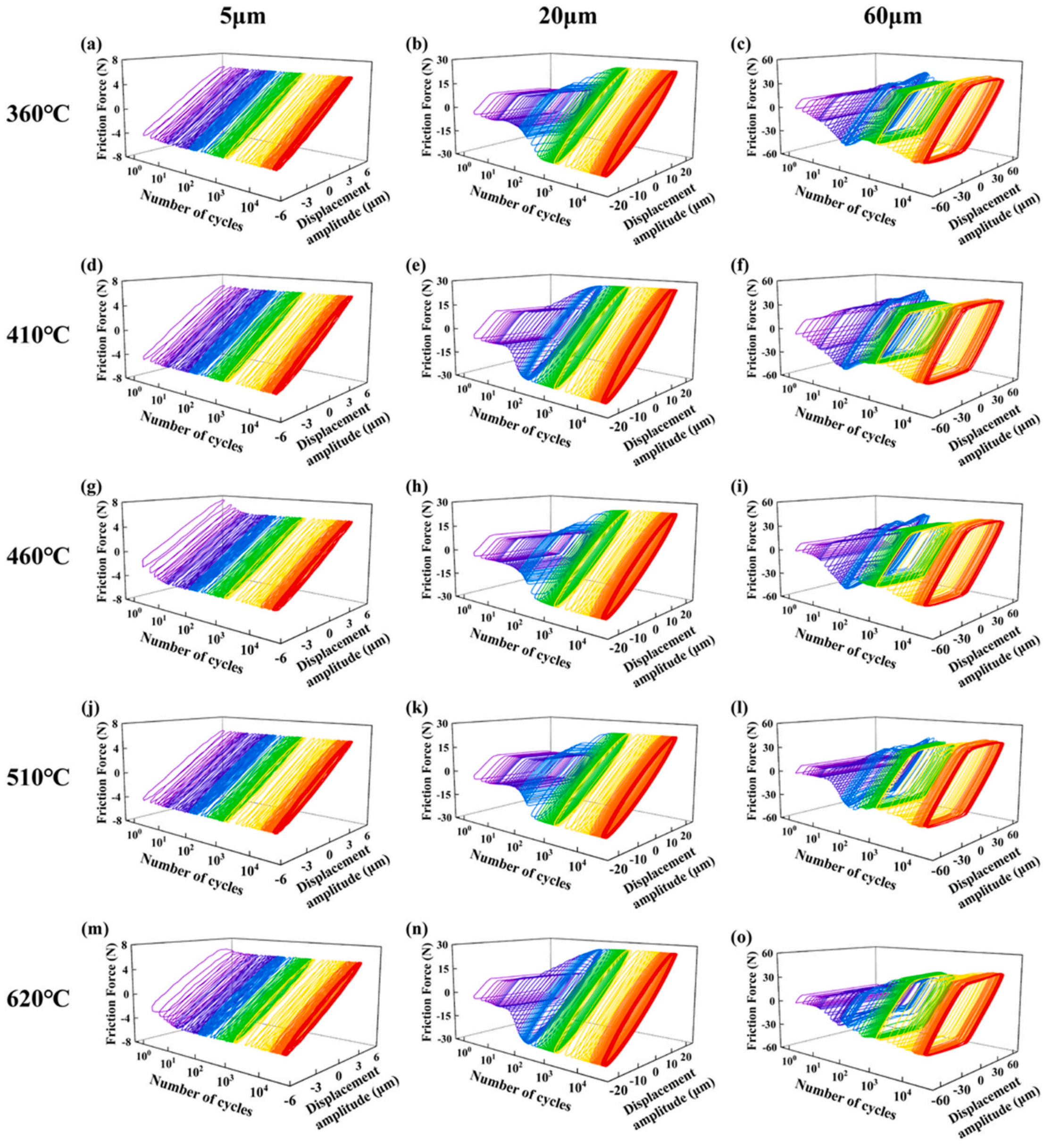

Fig. 9. The F_t-D-N curve evolutions of the 17-4 PH stainless steel under different aging temperature.

effect of contact interface. Given the relatively small displacement in MFR, therefore, the accommodated was mainly realized by elastoplastic deformation with a stick-slip motion, as a result showing elliptical loops. Moreover, in order to be further sure of the accuracy on the fretting regimes distinguishment by the F_t-D curve, the energy ratio A as proposed by Fouvry et al. [73] was utilized to confirm the fretting regime, which is defined as the ratio between the dissipated energy E_d for each F_t-D loop and the total energy E_t. Fig. 10 gives the calculated energy ratio A plotted as a function of cyclic number. It was stated by Fouvry et al. [73,74] that the energy ratio A of 0.2 could be regarded as the distinguished boundary between the partial slip state and the gross slip state. As can be seen, in the case of 5 μm displacement amplitude, the result of the ratio A for each cycle is located below 0.2, which illustrates that the fretting wear was running in PSR. While for the case of 60 μm, the value of energy ratio A for each cycle is above 0.2, which suggest that the fretting wear run in GSR. In contrast, in the case of 20 μm, the value of energy ration A fluctuated around the baseline of 0.2 at the stable stage, which refers to the MFR. It can be concluded that the criteria to distinguish the fretting wear region by energy ratio A and the shape of F_t-D curve more or less reach an agreement.

Moreover, Fig. 11 gives the stabilized coefficient of friction (CoF) of the samples with different aging temperature as a function of displace amplitude under the normal load of 60 N. It should be pointed out that the CoF is the defined as the ratio of F_t* and normal load F_n, where the F_t* is the average value of $F_{t,max}$ and absolute value of (-$F_{t,\max}$) for each cycle. It is clear that the stabilized friction coefficient rapidly increases with the increase of displacement amplitude up to 20 μm (i.e., in PSR and MFR), but show relatively slow increase in GSR (from 20 μm to 60 μm). In general, it seems that the aging temperature has little influence on the CoF.

3.5. Fretting wear results

Fig. 12 gives the fretting wear volumes of the samples subjected to varied aging temperature under different displacement amplitude. As can be seen, fretting wear resistance of PH stainless steels is strongly dependent on the aging temperature and the specific fretting run regime. In the case of PSR, due to the very small displacement amplitude, the wear damage is very mild and hence the wear volume is marginal. Among all samples, the sample T2 (410 °C) has a lowest fretting wear volume. In the MFR, the wear volume decreases with the aging temperature increases up to 410 °C, beyond which the wear volume commences to arise. The sample T2 (410 °C) still has a lowest wear volume, which may be related to its high hardness and UTS. The high strength can well resist the penetration of abrasives/indenter in PSR and MFR where the elastoplastic deformation is dominant. As the fretting wear run in GSR, the trend of wear volume with aging temperature is similar to that for MFR. However, the significant difference is that the lowest wear volume is the sample T3 (460 °C) in GSR, which could be due to its good balance of strength and ductility (seen in Fig. 8). While the largest wear volume is the sample T5 (620 °C). In GSR, the relative displacement is mainly accommodated by plastic deformation. The good combination of strength and ductility can impart a good capability to resist the penetration of abrasives/indenter and resist the initiation and propagation of cracks ductility due to plastic deformation accumulation. Therefore, the sample T3 (460 °C) has a best fretting wear resistance in GSR.

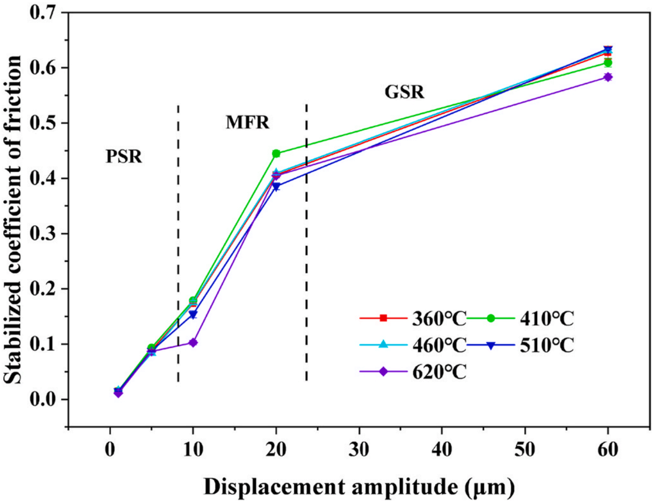

Fig. 11. The change of coefficient of friction with different displacement amplitudes for the 17-4 PH stainless steel at different aging temperature.

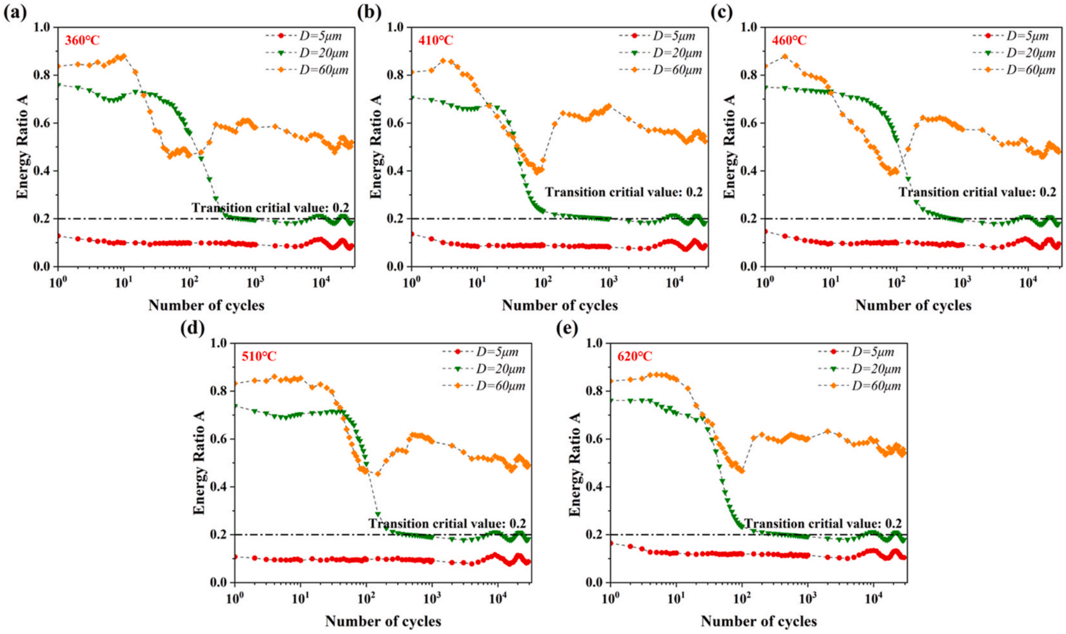

Fig. 10. The energy ratio A for the 17-4 PH stainless steel under different aging temperature.

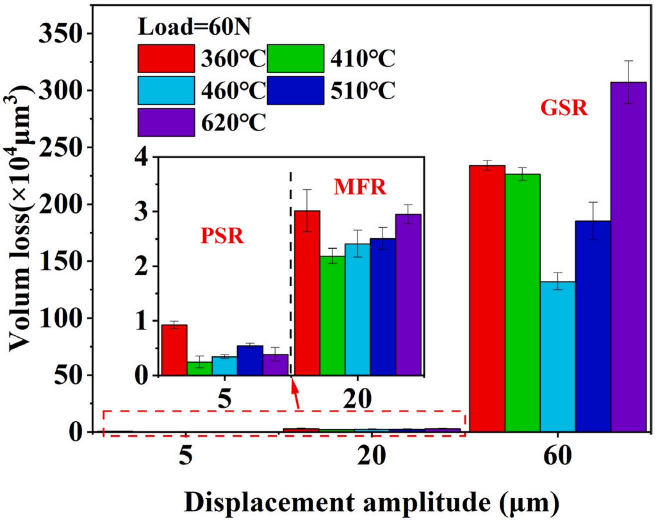

Fig. 12. The fretting wear volume of the 17-4 PH stainless steel with different aging temperature under different fretting running regimes.

3.6. *The morphologies of worn scars and failure mechanisms*

Fig. 13 presents the morphologies and the resulting profiles of worn scars in PSR or all samples under the normal load of 60 N. In PSR, the relative displacement imposed in PSR is accommodated by elastic deformation. According to Mindlin's theory [75], at the center of worn scar a maximum Hertzian contact pressure was formed, which can cause the stick state at the center region of the contact. Outwards from the center of worn scar, the Hertzian contact pressure gradually decreases, consequently resulting in a wear annulus around the outside edge of the contact zone. Therefore, a typical worn scar morphology of annularity was observed for all samples, as shown in Fig. 13(a, d, g, j, m). In order to further observe the wear damage, local magnified images of worn scars center were given in Fig. 13(b, e, h, k, n). It can be seen that the sample T2 (410 °C) and sample T3 (460 °C) both show no visible wear damage at the center of worn scars, especially for the sample T2 (410 °C). While for the rest sample, there are visible wear damage, such as debris, ploughing, and delamination, as shown in Fig. 13(b, k, n). In addition, the resulting profiles of worn scars well reflect the wear damage state of worn scars, as seen in Fig. 13(c, f, i, l, o). In general, the wear damage in SEM images was consisted with the results of wear volume in Fig. 12.

As the displace amplitude increases to 20 μm, the fretting wear run in MFR. The morphologies and the resulting profiles of worn scars for all samples were given in Fig. 14. Compared to the PSR, the worn scars of MFR show evident damage, and the sticking state remains at the center of contact interface. Among all samples, the center worn scar of sample T2 (410 °C) is relatively smooth with a small amount of delamination and craters. It can also be seen from Fig. 14(h) where the profile of worn scar is relatively flat with the lowest depth. With the increase in aging temperature, the delamination and craters become more serious. While for the sample T1 (360 °C), due to its lowest hardness, it also has severe delamination and craters along with ploughing. Moreover, on the edge of worn scars, all sample display evident cracks and delamination, which mostly created on the boundary of sticking region and edge region. As can be seen from the profiles of worn scars in Fig. 14(d, l, p, u), they show evident 'wave peak' referring to the chip and/or debris and 'wave trough' referring to the delamination and/or cracks.

In the case of GSR (D = 60 μm), the fretting wear damage of all samples becomes severe. As can be seen in Fig. 15, all worn scars mainly present serious delamination and craters as well as cracks. For the sample T1, due to its low hardness, the worn scar shows evident ploughing and cater as well as delamination, resulting in relatively high wear volume (seen in Fig. 12) and the large depth of worn scar (seen in Fig. 15(c)). Especially at the center region of worn scar, the profile of worn scar presents a deep and narrow 'wave trough', which can also be found for sample T2 (410 °C) and sample T4 (510 °C). It means that there is serious material damage at the center region, while the wear damage outwards from the center region is relatively mild. It could be due to the possibility that the higher contact stress at the center region makes the material surface more susceptible to serous plastic deformation and then brittle delamination and crack formation. In contrast, for the sample T5 (620 °C), due to the largest ductility and the lowest hardness, the microstructure is easy to be deformed and removed, hence showing a worn scar of a regular ball-shaped profile.

4. Discussions

4.1. *Dependence of fretting wear resistance on aging precipitation and fretting run regimes*

For precipitation-hardened steels, in industry aging heat treatment is often used to modify the microstructures so as to create promising combinations of strength and ductility [76–78]. As aging proceeds, there are three main differences in microstructures which alter the mechanical properties including the fretting wear resistance of 17-4 PH stainless steel [47,79]: 1) the reduction of residual stress and dislocation, 2) lath martensite coarsening, 3) the formation of precipitates. The multiple mechanisms could lead to non-monotonous correlation of strength/ductility and aging temperate [80]. Of importance is the precipitation formation which plays a significant role in determining the material strength depending on the aging temperature. At the aging temperature of 360 °C, a very fine dispersion of NbC precipitation was formed, as shown in Fig. 5(b). With increasing the aging temperature up to 410 °C and 460 °C, the amount of the NbC precipitation gradually arise, and new nano-CRPs (BCC) commenced to be formed at 460 °C (as seen in Fig. 6), consequently contributing to the increase of UTS and YS and reach the maximum at the 460 °C (as shown in Fig. 8). While for the hardness, the T3 (460 °C) specimen with new nano-CRPs (BCC) does not perform a highest hardness, which is lower than that for the T2 specimen (410 °C) without evident CRPs. This could be attributed the possibility that there are nano-scale Cu-rich clusters formed in microstructure under such relatively low aging temperature, yet it is failed to be probed with the TEM due to the quite small size. It can be supported from the work reported by Wang et al. [13,81]. It is pointed out that a significant number of Cu-rich clusters were formed in the 17-4 PH stainless steel after aging at 450 °C for 1 h [13] and at 420 °C for 4 h [81]. It is worth noting that the Cu-rich clusters (as a precursor for precipitation) are quite small and coherent aggregations of solute atoms, but not forming yet their own crystal structure [82]. They are different from the CRPs having their own crystal structure. Hence, it leads to a quite high hardness but low ductility for T2 specimen. However, with the aging temperature further increases up to 510 °C and 620 °C, as seen in Fig. 5 (h, k) and Fig. 7, the NbC and CRPs precipitates as well as the lath martensite become coarser, which will weaken the strengthening effect and hence lead to the decrease of the UTS and YS (seen in Fig. 8). Meanwhile, it is worth noting that the dominant phase of CRPs was evolved from BCC to 9 R and FCC(ε-Cu). Combining the result of Fig. 5, it seems that the BCC-CRPs has a better performance in improve the strength than the 9 R and FCC(ε-Cu) CRPs. Moreover, it is clear that after the CRPs formation, the ductility has a significant improvement, which may deduce that the CRPs formation is helpful to not only enhance the strength (depending on the aging temperature) but also improve the ductility. These microstructural changes certainly have their impact on the fretting wear behavior.

In PSR and MFR, the imposed displacement was mainly accommodated by elastic deformation and mainly regulated by elastic-plastic deformation, respectively [72]. Given that a higher hardness can well resist the elastic/plastic deformation (stress bearing capability) and even penetration of abrasives/indenter [83], a higher hardness of

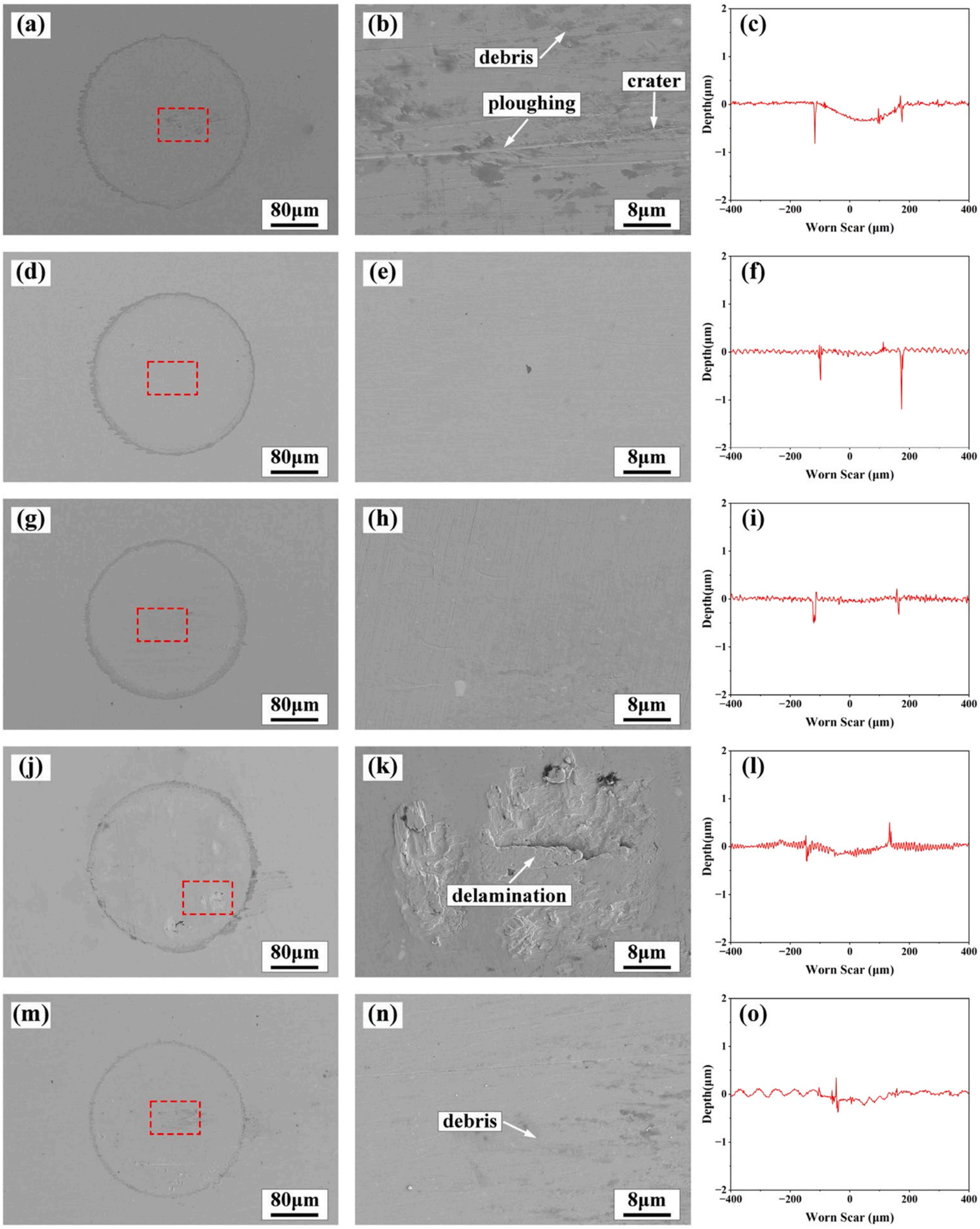

Fig. 13. SEM micrographs and the resulting 2D profile of the worn scars for the samples with different aging temperature in PSR ($D = 5$ μm): (a, b, c) 360 °C; (d, e, f) 410 °C; (g, h, i) 460 °C; (j, k, l) 510 °C; (m, n, o) 620 °C. Note: (b, e, h, k, n) are the local magnification of the red square as marked in (a, d, g, j, m), respectively.

microstructures can impart a better fretting wear resistance in PSR and MFR. It can well interpret that the sample T2 (410 °C) with a highest hardness due to strengthening effect of the fine NbC precipitates has a lowest wear volume, as shown in Fig. 8. In contrast, as the fretting ran in GSR, the samples show completely different wear resistance rank (as seen in Fig. 12), i.e., the lowest wear volume is the sample T3 (460 °C). In GSR, the contact surface material was suffered from the severe plastic deformation, accompanied by evident ploughing and delamination/cracks (as seen in Fig. 15). Hence, not only the strength (resisting penetration of indenter) but also the ductility (resisting crack initiation and propagation) is important for a material against the fretting wear in GSR. Upon aging treatment in the temperature of 460 °C, the combination of a fine dispersion of NbC and dominant BCC-CRPs with a hard matrix imparts a good balance of strength and ductility (as seen in Fig. 8), consequently resulting in a highest fretting wear resistance of sample T3 (460 °C). Moreover, compared with the T2 sample without CRPs, the sample T3 and T4 with CRPs have lower wear volume (seen in Fig. 12). It can be concluded that the formation of fine CRPs plays a positive role in improving the fretting wear resistance. In particular the sample T3 with dominant BCC-CRPs, it has a better performance against fretting wear than the sample T4 (510 °C) with dominant 9 R-CRPs, i.e., showing a best fretting wear resistance among all samples. It may suggest that the BCC-CRPs has a better enhancement effect on fretting wear resistance than the 9 R-CRPs. As the aging temperature further increased up to the 620 °C, the precipitates became coarse and evolved to FCC (ε-Cu). Combining the result of Fig. 12 where the sample T5 (620 °C) has a largest wear volume, it indicates that coarse ε-Cu precipitates deteriorate the fretting wear resistance. As a result, the wear volume gradually increased and reach the maximum at the temperature of 620 °C. The results as discussed above clearly point out that the formation of precipitates resulting from the aging treatment plays a vital role in determining the fretting wear behavior and associated damage mechanisms, which is dependent on the fretting run regimes.

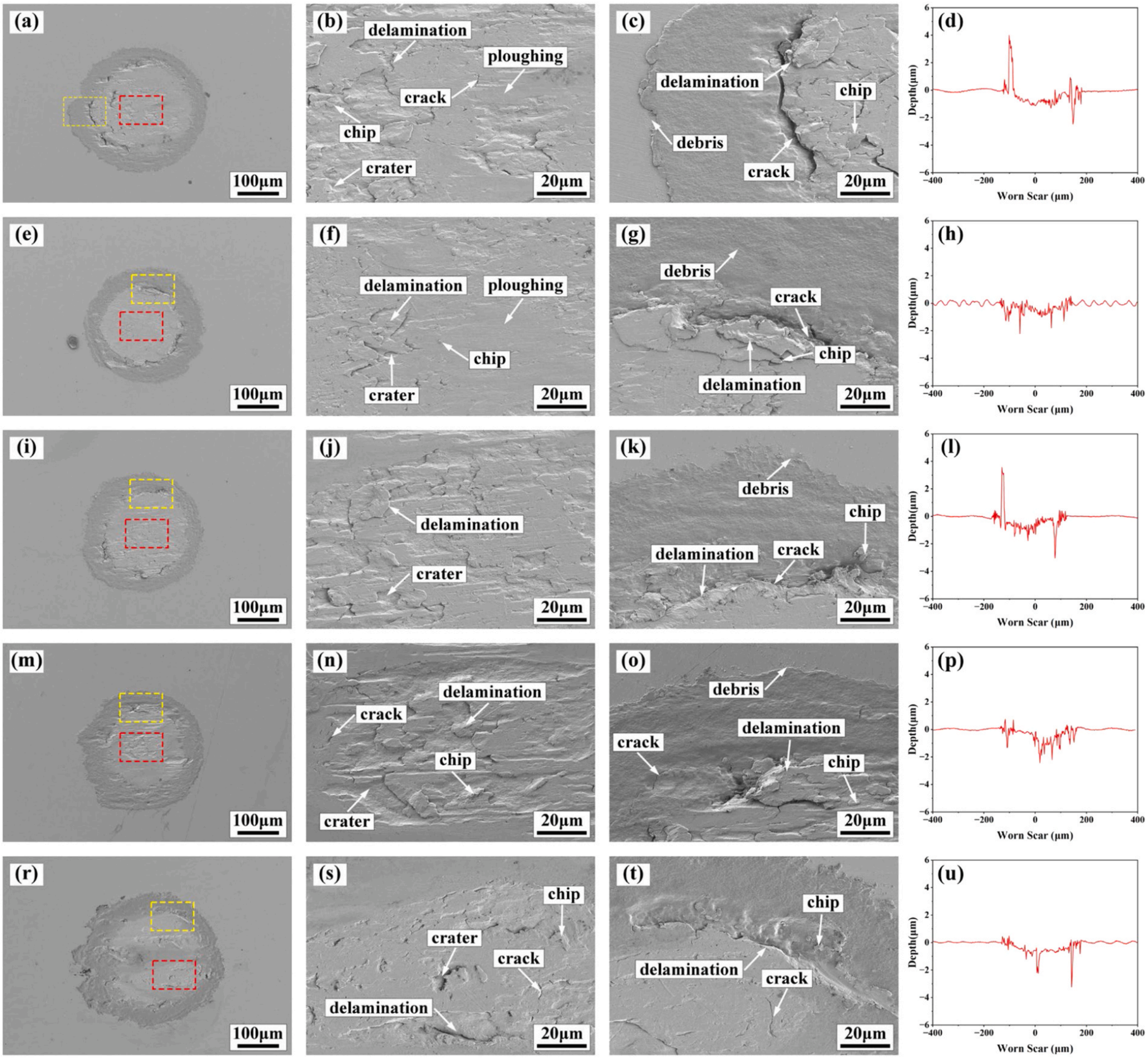

Fig. 14. SEM micrographs and the resulting 2D profile of the worn scars of MFR (D = 20 μm) for all aging temperature: (a, b, c, d) 360 °C; (e, f, g, h) 410 °C; (i, j, k, l) 460 °C; (m, n, o, p) 510 °C; (r, s, t, u) 620 °C. Note: (b, f, j, n, s) and (c, g, k, o, t) are the local magnification of the red and yellow square as marked in (a, e, i, m, r), respectively.

4.2. The development of plastic deformation layer

During continuous wear process, the surface material will be deformed plastically upon the external force and then create a plastic deformation layer, which is the actual component against the fretting wear during wear process, consequently controlling the wear performance for a metallic material. To clarify the correlation between the development of plastic deformation layer and fretting wear resistance, the worn scars of different fretting run regimes were cut perpendicular to the wear direction, and the resulting subsurface were investigated by SEM. Figs. 16–18 give the resulting images of plastic deformation layer. It should be noted that in order to be better reveal the subsurface microstructural response with regard to the highest and lowest wear resistance, the samples of 360 °C, 410 °C (460 °C for GSR), 620 °C of each fretting run regime were selected to be further observed, respectively. It is clear that the microstructure beneath the surface was modified and produce plastic deformation expanded to different thickness depending on the fretting run regimes.

In the PSR, given nearly no relative slip between the contact interface (seen in Fig. 13), there is no visible plastic deformation layer produced on the top of subsurface for all samples as seen in Fig. 16, hence showing a very little wear volume. However, with the further increase of displacement amplitude entering to the MFR (D = 20 μm), there is an evident plastic deformation layer on the top of subsurface, as seen in Fig. 17. In addition, the EDS results of O element along the depth direction is also given so as to correlate with the tribo-oxidation. As can be seen, the sample T2 (410 °C) has an equivalent thickness of plastic deformation layer to that for the sample T1 (360 °C). Nonetheless, the subsurface for the sample T1 (360 °C) has lots of ‘pits’, which can promote the crack nucleation and propagation upon plastic deformation. In contrast, the sample T2 (410 °C) shows a more compacted plastic deformation layer without evident ‘pits’, but involve an evident oxide layer on the top subsurface (seen in Fig. 17(d)), hence leading to a better wear resistance. While for the sample T5 (620 °C), due to its lowest tensile strength but largest ductility (seen in Fig. 8), it is susceptible to be deformed plastically and hence created a thickest plastic deformation layer, as observed in Fig. 17(e). As the plastic deformation reached the limitation, the microstructure became brittle and then the cracks were formed, consequently resulting in material removal/damage and hence showing a highest wear volume. That is consisted with the observation in Fig. 14(s, t) in which evident cracks and delamination can be investigated. In addition, the EDS result as shown in Fig. 17(f) demonstrate

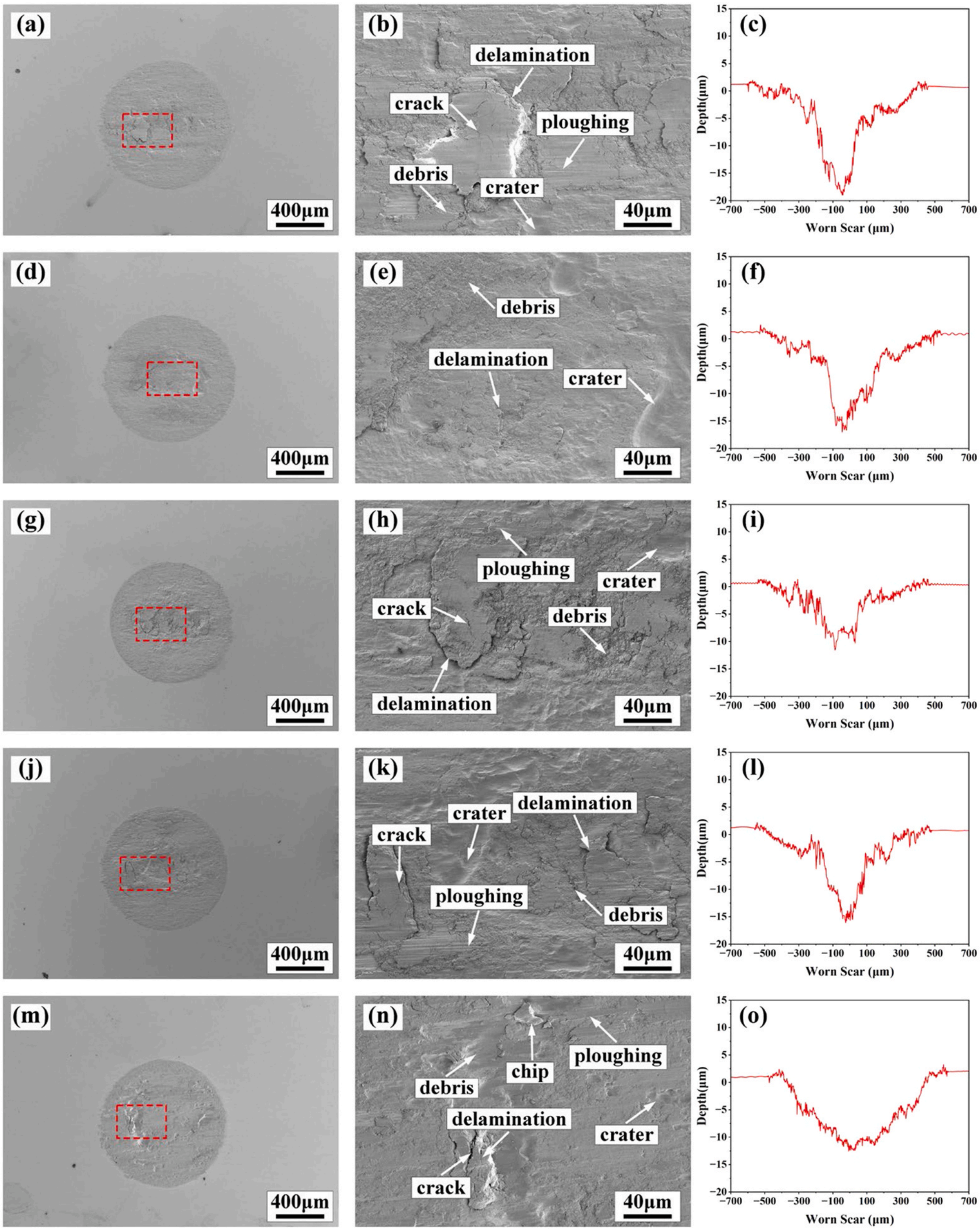

Fig. 15. SEM micrographs and the resulting 2D profile of the worn scars of GSR (D = 60 μm) for all aging temperature: (a, b, c) 360 °C; (d, e, f) 410 °C; (g, h, i) 460 °C; (j, k, l) 510 °C; (m, n, o) 620 °C. Note: (b, e, h, k, n) are the local magnification of the red square as marked in (a, d, g, j, m), respectively.

that on the top subsurface there is no evident tribological oxidation layer.

Fig. 18 gives the SEM micrographs of subsurface for the samples of 360 °C, 460 °C and 620 °C in GSR(D = 60 μm). In comparison to MFR, the plastic deformation layer became broader due to severe plastic deformation in GSR. Among the three samples, the sample T3 (460 °C) has a thickest plastic deformation layer, compared to the sample T1 and sample T5. For the sample T3 (460 °C), it is clear that a thick mechanical mixture layer (MML) was generated on the top of the subsurface, which could be the result of wear debris agglomeration and plastic deformation, hence also explaining the pits formation as indicated in Fig. 18(c) [84]. In addition, the corresponding EDS result demonstrates that there are evident tribo-oxides formed in MML (seen in Fig. 18(d)). As reported in Refs. [84,85], a continuous, thick and oxide-contained MML could play an effective protection role against wear, consequently leading to a high fretting wear resistance for the sample T3 (460 °C). At the steady stage of fretting wear, in general, a dynamic equilibrium of plastic-deformation layer development and removal will be established. Based on the observation of microstructural features, CRPs (BCC) stared to be formed when the aging temperature increases up to 460 °C (T3). Combined with the result of Fig. 8, the ductility has a significant improvement for T3 sample at 460 °C of aging temperature, which could be due to the CRPs formation. On the one hand, the improvement of ductility can impart a good capability of plastic deformation, hence being easy to production of plastic-deformation layer. On the other hand, high ductility will cause the decrease in strength, which can accelerate the removal of materials. In contrast, for the T3 (460 °C) sample, it has not only highest UTS but also high ductility. Therefore, the production of plastic-deformation layer is dominant for T3 sample, which may suggest that the existence of the BCC-CRPs could promote the formation of thick and oxide-contained plastic deformation layer. In contrast, the sample T1 and sample T5 both have relatively thin plastic deformation layer without visible MML and tribo-oxide layer. It implies that the subsurface removal is dominant comparing to subsurface

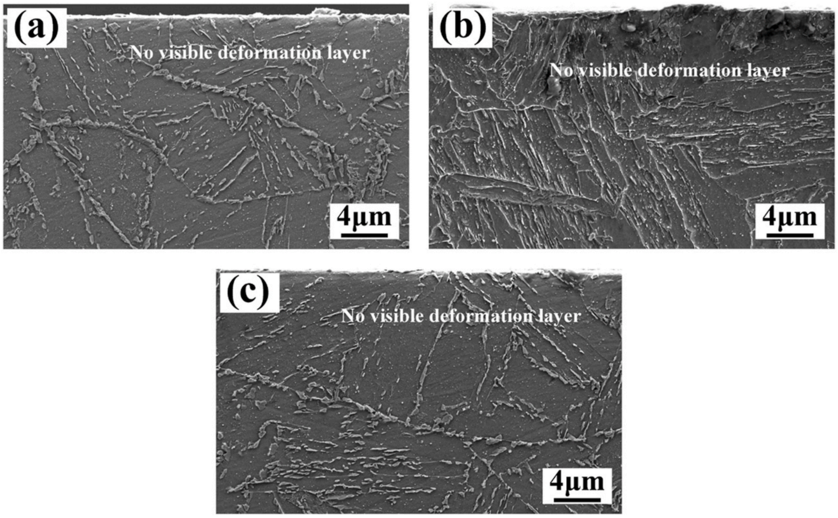

Fig. 16. SEM micrographs of subsurface for 17-4 PH stainless steel with different aging temperature at PSR (D = 5 μm): (a) 360 °C; (b) 410 °C; (c) 620 °C.

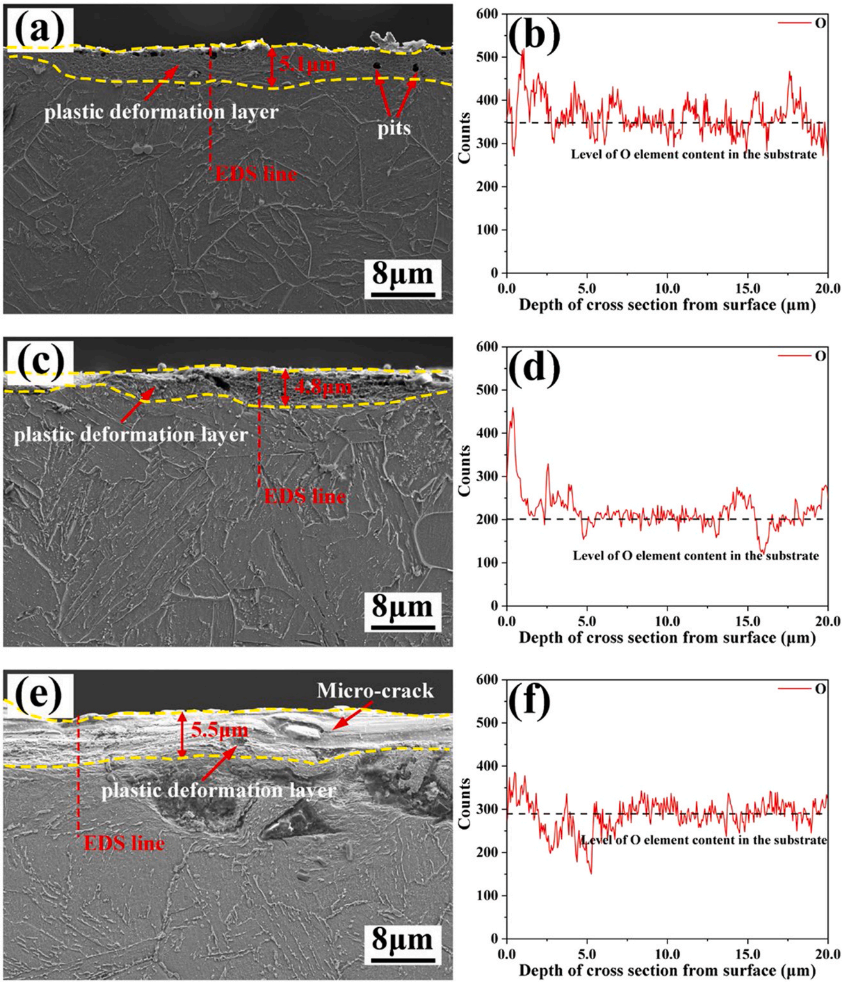

Fig. 17. SEM micrographs and EDS results of subsurface for 17-4 PH stainless steel with different aging temperature at MFR (D = 20 μm): (a) 360 °C; (c) 410 °C; (e) 620 °C.Note: (b, d, f) are the EDS line scan results of O element along the depth direction in the cross section in (a, c, e), respectively.

development, hence resulting in a much high wear volume. Moreover, because of the largest ductility and the lowest hardness, for the sample T5, an evident band microstructure can be found, which was teared along the sliding direction, as indicated in Fig. 18(e). Upon the subsequent fretting wear event, the deformed microstructure was frequently extruded with the accumulation of plastic deformation, which make it easy to generate the cracks, as indicated in Fig. 18(e). It is also consisted with the observation of worn scars in Fig. 15 where the

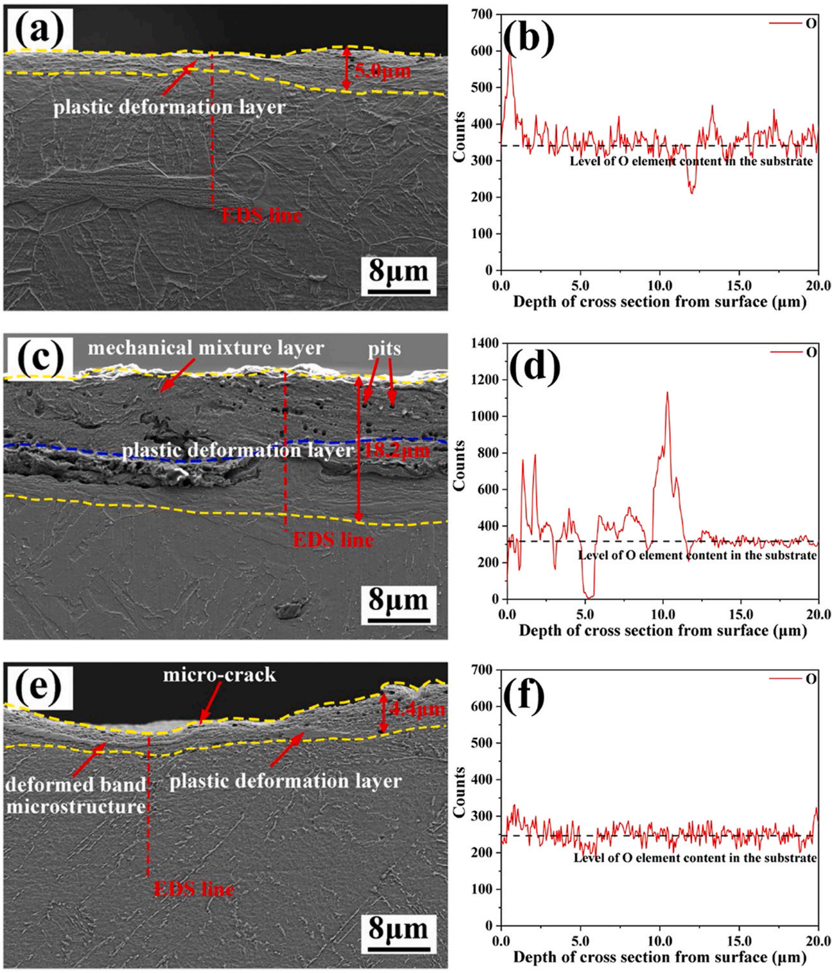

Fig. 18. SEM micrographs and EDS results of subsurface for 17-4 PH stainless steel with different aging temperature at GSR (D = 60 μm): (a) 360 °C; (c) 460 °C; (e) 620 °C.Note: (b, d, f) are the EDS line scan results of O element along the depth direction in the cross section in (a, c, e), respectively.

serious delamination and cracks can be found. In addition, no evident tribo-oxides can be found on the top of subsurface, as seen in Fig. 18(f). As a result, the sample T5 has a largest wear volume (seen in Fig. 12).

5. Conclusions

In the present work, the fretting wear behavior of a 17-4 PH stainless steel subjected to different aging heat treatments and the response of precipitate variants and plastic deformation layer on the fretting wear resistance were studied. Results show that the precipitates due to aging treatment have significant influence on fretting wear resistance depending on the fretting running regime. The following conclusions can be drawn.

(1) The microstructure is consisted of a typical martensitic lath and some δ-ferrite, along with different precipitate variants. At and below 410 °C of aging temperature, the precipitates are mainly NbC. Above 410 °C, not only NbC but also CRPs start to be formed. The dominant CRPs evolve from BCC phase to 9 R phase, and finally to FCC (ε-Cu) phase with the aging temperature increases from 460 °C, 510 °C, to 620 °C, respectively.

(2) The Hv, YS and UTS firstly increase and then decrease with the aging temperature increases, but the TE shows an opposite trend. The CRPs formation is helpful to improve the TE.

(3) In the PSR and MFR, the fretting wear volume decreases with the aging temperature increases up to 410 °C, beyond which the wear volume commences to arise. The sample T2 (410 °C) has a highest fretting wear resistance. In GSR, the fretting wear volume shows a similar trend with aging temperature, but the sample T3 (460 °C) has a highest fretting wear resistance. The results can offer a guideline to optimize the target microstructure for a specific working condition or tune the working condition parameter to allow a best fretting wear resistance.

(4) The observations of plastic deformation layer demonstrate that a compacted and oxide-contained plastic deformation layer has a good performance to resist fretting wear. The presence of BCC-CRPs may promote the formation of a compacted and oxide-contained plastic deformation layer, and has a better enhancement effect on fretting wear resistance.

CRediT authorship contribution statement

Xiaojun Xu: Conceptualization, Methodology, Writing – review & editing, Supervision, Funding acquisition. Binbin Gan: Conceptualization, Methodology, Investigation, Writing - original draft, Writing – review & editing. Ting Yang: Writing – review & editing, Formal analysis. Xiaoqin Zha: Conceptualization, Methodology, Supervision, Project administration, Funding acquisition. Jianjun Long: Conceptualization, Writing – review & editing. Xiaoyu Zhang: Methodology, Formal analysis. Pingyang He: Investigation, Formal analysis. Hao Li: Methodology, Formal analysis. Minhao Zhu: Supervision, Funding acquisition.

Funding

This work was supported by Research Fund of National Key Laboratory of Marine Corrosion and Protection of Luoyang Ship Material Research Institute (JCJQ-JJ23004) and National Natural Science Foundation of China (52171079).

Declaration of competing interest

The authors declare that they have no known competing financial interests or personal relationships that could have appeared to influence the work reported in this paper.

Acknowledgment

The authors gratefully acknowledge financial supported by the Research Fund of National Key Laboratory of Marine Corrosion and Protection of Luoyang Ship Material Research Institute (JCJQ-JJ23004), and supported by the National Natural Science Foundation of China (52171079).

Data availability

Data will be made available on request. Please contact the corresponding author for access to the data.

References

[1] Provines JT. Specified pretension values and installation parameters for 2205 and 17–4 PH condition H1150 stainless steel fastener assemblies. J Constr Steel Res 2023;210:108052. https://doi.org/10.1016/j.jcsr.2023.108052.

[2] Srinath J, Manwatkar SK, Narayana Murty SVS, Ramesh Narayanan P, Sharma SC, George KM. Metallurgical analysis of a failed 17-4 PH stainless steel pyro bolt used in launch vehicle separation systems. Mater Perform Charact 2015;4:29–44. https://doi.org/10.1520/MPC20140063.

[3] Peng JF, Zhao YG, Chen RL, Song Y, Zhong ZY, Liu JH, et al. Study on bending fretting fatigue behaviour of 15-5PH stainless steel with different fretting regimes. Tribol Int 2024;194:109566. https://doi.org/10.1016/j.triboint.2024.109566.

[4] Villegas-Tovar J, Gaona-Tiburcio C, Lara-Banda M, Maldonado-Bandala E, Baltazar-Zamora MA, Cabral-Miramontes J, et al. Electrochemical corrosion behavior of passivated precipitation hardening stainless steels for aerospace applications. Metals 2023;13:835. https://doi.org/10.3390/met13050835.

[5] Arisoy CF, Başman G, Şeşen MK. Failure of a 17-4 PH stainless steel sailboat propeller shaft. Eng Fail Anal 2003;10:711–7. https://doi.org/10.1016/S1350-6307(03)00041-4.

[6] Bellezze T, Roventi G, Fratesi R. Localised corrosion and cathodic protection of 17 4PH propeller shafts. Corros Eng Sci Technol 2013;48:340–5. https://doi.org/10.1179/1743278213Y.0000000082.

[7] Uddin MJ, Siller HR, Mirshams RA, Byers TA, Rout B. Effects of proton irradiation on nanoindentation strain-rate sensitivity and microstructural properties in L-PBF 17–4 PH stainless steels. Mater Sci Eng A 2022;837:142719. https://doi.org/10.1016/j.msea.2022.142719.

[8] Lee J, Park G, Oh CY, Son Y, Kim S, Bahn CB. Effects of long-term thermal aging on mechanical properties and microstructural evolution of 17–4 PH stainless steel in simulated thermal conditions for nuclear applications. J Nucl Mater 2025;606:155628. https://doi.org/10.1016/j.jnucmat.2025.155628.

[9] Habibi Bajguirani HR. The effect of ageing upon the microstructure and mechanical properties of type 15-5 PH stainless steel. Mater Sci Eng A 2002;338:142–59. https://doi.org/10.1016/S0921-5093(02)00062-X.

[10] Hsiao CN, Chiou CS, Yang JR. Aging reactions in a 17-4 PH stainless steel. Mater Chem Phys 2002;74:134–42. https://doi.org/10.1016/S0254-0584(01)00460-6.

[11] Shaffer DJ, Wilson-Heid AE, Keist JS, Beese AM, Palmer TA. Impact of retained austenite on the aging response of additively manufactured 17-4 PH grade stainless steel. Mater Sci Eng A 2021;817:141363. https://doi.org/10.1016/j.msea.2021.141363.

[12] LeBrun T, Nakamoto T, Horikawa K, Kobayashi H. Effect of retained austenite on subsequent thermal processing and resultant mechanical properties of selective laser melted 17–4 PH stainless steel. Mater Des 2015;81:44–53. https://doi.org/10.1016/j.matdes.2015.05.026.

[13] Wang Z, Li H, Shen Q, Liu W, Wang Z. Nano-precipitates evolution and their effects on mechanical properties of 17-4 precipitation-hardening stainless steel. Acta Mater 2018;156:158–71. https://doi.org/10.1016/j.actamat.2018.06.031.

[14] Ozsoy A, Aydogan E, Dericioglu AF. Selective laser melting of Nano-TiN reinforced 17-4 PH stainless steel: densification, microstructure and mechanical properties. Mater Sci Eng A 2022;836:142574. https://doi.org/10.1016/j.msea.2021.142574.

[15] Waterhouse RB. Fretting corrosion. Oxford: Pergamon Press; 1972.

[16] Waterhouse RB. Fretting fatigue. London: AppliedScience Publishers; 1981.

[17] Vincent L, Berthier Y, Dubourg MC, Godet M. Mechanics and materials in fretting. Wear 1992;153:135–48. https://doi.org/10.1016/0043-1648(92)90266-B.

[18] Imran M, Wang D, Wang L, Abdel Wahab M. Finite element modelling of effect of corrosion on fretting wear in steel wires. Tribol Int 2025;206:110573. https://doi.org/10.1016/j.triboint.2025.110573.

[19] Fang X, Wang Z, Wahab MA, Gong J, Liu X, Liu X, et al. Fretting wear mechanism of GH4169 dovetail joint specimens treated with hybrid laser shock peening. Tribol Int 2025;209:110740. https://doi.org/10.1016/j.triboint.2025.110740.

[20] Wang G, Peng Y, Zhu Z, Chang X, Lu H, Wang D, et al. A multi-physics coupling analysis to predict stress corrosion characteristics of wires in rope under wear damage. Simul Model Pract Theory 2024;131:102882. https://doi.org/10.1016/j.simpat.2023.102882.

[21] Li C, Amanov A, Wang C, Wang L, Abdel Wahab M. Effect of laser shock peening on fretting wear behaviour of AISI 304 stainless alloy. Tribol Int 2024;193:109386. https://doi.org/10.1016/j.triboint.2024.109386.

[22] Imran M, Wang D, Zhou Y, Wang L, Abdel Wahab M. Simulation of fretting wear in steel wires under variable coefficient of friction and variable wear coefficient. Simul Model Pract Theory 2024;134:102959. https://doi.org/10.1016/j.simpat.2024.102959.

[23] Xu X, Long J, Zhang X, Dong Y, Gan B, Li H, et al. Dependence of fretting wear resistance on the α morphology and stress-induced martensite transformation in a metastable β titanium alloy. J Alloy Compd 2025;1010:177259. https://doi.org/10.1016/j.jallcom.2024.177259.

[24] Liu D, Liu DX, Zhang XH, He GY, Ma A, Wu GT. Plain fatigue and fretting fatigue behaviors of 17-4PH steel subjected to ultrasonic surface rolling process: a comparative study. Surf Coat Technol 2020;399:126196. https://doi.org/10.1016/j.surfcoat.2020.126196.

[25] Anton DL, Lutian MJ, Favrow LH, Logan D, Annigeri B. The effects of contact stress and slip distance on fretting fatigue damage in Ti-6Al-4V/17-4PH contacts. In: Hoeppner DW, Chandrasekaran V, Elliott C, editors. Fretting fatigue: current technology and practices. ASTM International; 2000. p. 119–40.

[26] Pape J, Neu R. A comparative study of the fretting fatigue behavior of 4340 steel and PH 13-8 Mo stainless steel. Int J Fatig 2007;29:2219–29. https://doi.org/10.1016/j.ijfatigue.2006.12.016.

[27] Pape JA, Neu RW. Subsurface damage development during fretting fatigue of high strength steel. Tribol Int 2007;40:1111–9. https://doi.org/10.1016/j.triboint.2006.10.009.

[28] Liu D, Liu D, Zhang X, Liu C, Ma A, Xu X, et al. An investigation of fretting fatigue behavior and mechanism in 17-4PH stainless steel with gradient structure produced by an ultrasonic surface rolling process. Int J Fatig 2020;131:105340. https://doi.org/10.1016/j.ijfatigue.2019.105340.

[29] Waterhouse RB. Fretting fatigue. Int Mater Rev 1992;37:77–98. https://doi.org/10.1179/imr.1992.37.1.77.

[30] Liu RL, Yan MF. The microstructure and properties of 17-4PH martensitic precipitation hardening stainless steel modified by plasma nitrocarburizing. Surf Coat Technol 2010;204:2251–6. https://doi.org/10.1016/j.surfcoat.2009.12.016.

[31] Han Z, Lu J, Yin C, Lai P, Zhuang W, Li L, et al. Composition, microstructure, and phase evolution of 17-4PH stainless steel with a work-hardened layer in the low-temperature plasma nitriding process. Surf Coat Technol 2022;451:128950. https://doi.org/10.1016/j.surfcoat.2022.128950.

[32] Liu D, Liu D, Wu Y, Yang J, Xu X, Li M, et al. Insight into nitriding behavior and corrosion mechanism in 17-4PH steel: the influence of nanocrystalline structure. J Mater Res Technol 2023;27:3761–76. https://doi.org/10.1016/j.jmrt.2023.10.324.

[33] Han Z, Zhuang W, Lai P, Wang J, Guo X, Zhang L. General corrosion behavior and mechanism of low-temperature plasma nitrided 17–4PH stainless steel in high temperature water. Mater Char 2024;209:113702. https://doi.org/10.1016/j.matchar.2024.113702.

[34] Han Z, Zhuang W, Lai P, Wang J, Zhang L, Guo X. Effect of low-temperature plasma nitriding on the sliding wear behavior of 17–4PH stainless steel in high temperature water. Mater Today Commun 2024;40:110062. https://doi.org/10.1016/j.mtcomm.2024.110062.

[35] Qi F, Leng YX, Huang N, Bai B, Zhang PC. Surface modification of 17-4PH stainless steel by DC plasma nitriding and titanium nitride film duplex treatment. Nucl Instrum Methods Phys Res Sect B 2007;257:416–9. https://doi.org/10.1016/j.nimb.2007.01.087.

[36] Walczak M, Szala M. Effect of shot peening on the surface properties, corrosion and wear performance of 17-4PH steel produced by DMLS additive manufacturing. Arch Civ Mech Eng 2021;21:157. https://doi.org/10.1007/s43452-021-00306-3.

[37] Swietlicki A, Walczak M, Szala M. Effect of shot peening on corrosion resistance of additive manufactured 17-4PH steel. Mater Sci 2022;40:135–51. https://doi.org/10.2478/msp-2022-0038.

[38] Walczak M, Świetlicki A, Szala M, Turek M, Chocyk D. Shot peening effect on sliding wear in 0.9% NaCl of additively manufactured 17-4PH steel. Materials 2024;17:1383. https://doi.org/10.3390/ma17061383.

[39] Sarkar S, Mukherjee S, Kumar CS, Kumar Nath A. Effects of heat treatment on microstructure, mechanical and corrosion properties of 15-5 PH stainless steel parts built by selective laser melting process. J Manuf Process 2020;50:279–94. https://doi.org/10.1016/j.jmapro.2019.12.048.

[40] Sabooni S, Chabok A, Feng SC, Blaauw H, Pijper TC, Yang HJ, et al. Laser powder bed fusion of 17–4 PH stainless steel: a comparative study on the effect of heat treatment on the microstructure evolution and mechanical properties. Addit Manuf 2021;46:102176. https://doi.org/10.1016/j.addma.2021.102176.

[41] Huang R, Zhao H, Sun Y, Lin D, Tang Z, Chen B, et al. Additive manufacturing of 17-4PH stainless steel: effect of heat treatment on microstructure evolution and

strengthening behavior. Mater Sci Eng A 2024;908:146770. https://doi.org/10.1016/j.msea.2024.146770.

[42] Sun Y, Zhong Y, Wang L. The interaction between ε-copper and dislocation in a high copper 17-4PH steel. Mater Sci Eng A 2019;756:319–27. https://doi.org/10.1016/j.msea.2019.03.092.

[43] Wei B, Niu M, Cai Z, Xu J, Sun C, Wang W, et al. Cu-rich nano precipitates simultaneously enhance the tensile properties, antibacterial efficacy, and corrosion resistance of ultra-high strength steel. Acta Mater 2025;292:121026. https://doi.org/10.1016/j.actamat.2025.121026.

[44] Chen Z, Zhou G, Chen Z. Microstructure and hardness investigation of 17-4PH stainless steel by laser quenching. Mater Sci Eng A 2012;534:536–41. https://doi.org/10.1016/j.msea.2011.12.004.

[45] Goodman SR, Brenner SS, Low JR. An FIM-Atom probe study of the precipitation of copper from lron-1.4 at. pct copper. Part II: atom probe analyses. Metall Trans 1973;4:2371–8. https://doi.org/10.1007/BF02669377.

[46] Goodman SR, Brenner SS, Low JR. An FIM-atom probe study of the precipitation of copper from lron-1.4 at. pct copper. Part I: Field-ion microscopy. Metall Trans 1973;4:2363–9. https://doi.org/10.1007/BF02669376.

[47] Viswanathan UK, Banerjee S, Krishnan R. Effects of aging on the microstructure of 17-4 PH stainless steel. Mater Sci Eng A 1988;104:181–9. https://doi.org/10.1016/0025-5416(88)90420-X.

[48] Othen PJ, Jenkins ML, Smith GDW, Phythianj WJ. Transmission electron microscope investigations of the structure of copper precipitates in thermally-aged fe-cu and fe-cu-ni. Philos Mag Lett 1991;64:383–91. https://doi.org/10.1080/09500839108215121.

[49] Othen PJ, Jenkins ML, Smith GDW. High-resolution electron microscopy studies of the structure of Cu precipitates in α-Fe. Philos Mag A 1994;70:1–24. https://doi.org/10.1080/01418619408242533.

[50] Monzen R, Iguchi M, Jenkins ML. Structural changes of 9R copper precipitates in an aged Fe-Cu alloy. Philos Mag Lett 2000;80:137–48. https://doi.org/10.1080/095008300176263.

[51] Monzen R, Jenkins ML, Sutton AR. The bcc-to-9R martensitic transformation of Cu precipitates and the relaxation process of elastic strains in an Fe-Cu alloy. Philos Mag A 2000;80:711–23. https://doi.org/10.1080/01418610008212077.

[52] Liu D, Liu D, Zhang X, Ma A, Liu C. Microstructural evolution mechanisms in rolled 17-4PH steel processed by ultrasonic surface rolling process. Mater Sci Eng A 2020;773:138720. https://doi.org/10.1016/j.msea.2019.138720.

[53] Conde FF, Escobar JD, Oliveira JP, Jardini AL, Bose Filho WW, Avila JA. Austenite reversion kinetics and stability during tempering of an additively manufactured maraging 300 steel. Addit Manuf 2019;29:100804. https://doi.org/10.1016/j.addma.2019.100804.

[54] Escobar JD, Faria GA, Wu L, Oliveira JP, Mei PR, Ramirez AJ. Austenite reversion kinetics and stability during tempering of a Ti-stabilized supermartensitic stainless steel: correlative in situ synchrotron x-ray diffraction and dilatometry. Acta Mater 2017;138:92–9. https://doi.org/10.1016/j.actamat.2017.07.036.

[55] Ma XP, Wang LJ, Liu CM, Subramanian SV. Microstructure and properties of 13Cr5Ni1Mo0.025Nb0.09V0.06N super martensitic stainless steel. Mater Sci Eng A 2012;539:271–9. https://doi.org/10.1016/j.msea.2012.01.093.

[56] Leem D-S, Lee Y-D, Jun J-H, Choi C-S. Amount of retained austenite at room temperature after reverse transformation of martensite to austenite in an Fe–13% Cr–7%Ni–3%Si martensitic stainless steel. Scr Mater 2001;45:767–72. https://doi.org/10.1016/S1359-6462(01)01093-4.

[57] Zhang Y, Lv J, Ji H, Lv C, Zhong Y, Liu Q, et al. In situ observation of high temperature microstructure and reverted austenite evolution in 13Cr supermartensitic stainless steel. Mater Res Express 2019;6:1265j9. https://doi.org/10.1088/2053-1591/ab71c7.

[58] Nishiyama Z. Martensitic transformation. New York: Academic Press; 1978.

[59] Yuan X, Li G, Zhang X, Pu J, Ren P. An experimental investigation on fretting wear behavior of copper–magnesium alloy. Wear 2020;462–463:203497. https://doi.org/10.1016/j.wear.2020.203497.

[60] Li S, Eliniyaz Z, Zhang L, Sun F, Shen Y, Shan A. Microstructural evolution of delta ferrite in SAVE12 steel under heat treatment and short-term creep. Mater Char 2012;73:144–52. https://doi.org/10.1016/j.matchar.2012.08.009.

[61] Raghuraman V, Kumar TS. The impact of different heat treatments on the surface characteristics, residual stresses, and tensile strength of maraging steel 1.2709 samples produced by LPBF. Results Eng 2025;26:105509. https://doi.org/10.1016/j.rineng.2025.105509.

[62] Sathyanath A, Meena A. Microstructural evolution and strain hardening behavior of heat-treated 17-4 PH stainless steel. Mater Today Commun 2020;25:101416. https://doi.org/10.1016/j.mtcomm.2020.101416.

[63] Shi ZM, Gong W, Tomota Y, Harjo S, Li J, Chi B, et al. Study of tempering behavior of lath martensite using in situ neutron diffraction. Mater Char 2015;107:29–32. https://doi.org/10.1016/j.matchar.2015.06.040.

[64] Yan Z, Liu K, Eckert J. Effect of tempering and deep cryogenic treatment on microstructure and mechanical properties of cr–mo–v–ni steel. Mater Sci Eng A 2020;787:139520. https://doi.org/10.1016/j.msea.2020.139520.

[65] Li K, Zhan J, Yang T, To AC, Tan S, Tang Q, et al. Homogenization timing effect on microstructure and precipitation strengthening of 17–4PH stainless steel fabricated by laser powder bed fusion. Addit Manuf 2022;52:102672. https://doi.org/10.1016/j.addma.2022.102672.

[66] Yeli G, Auger MA, Wilford K, Smith GDW, Bagot PAJ, Moody MP. Sequential nucleation of phases in a 17-4PH steel: microstructural characterisation and mechanical properties. Acta Mater 2017;125:38–49. https://doi.org/10.1016/j.actamat.2016.11.052.

[67] Wen YR, Hirata A, Zhang ZW, Fujita T, Liu CT, Jiang JH, et al. Microstructure characterization of Cu-rich nanoprecipitates in a Fe–2.5 Cu–1.5 Mn–4.0 Ni–1.0 Al multicomponent ferritic alloy. Acta Mater 2013;61:2133–47. https://doi.org/10.1016/j.actamat.2012.12.034.

[68] Han G, Xie ZJ, Xiong L, Shang CJ, Misra RDK. Evolution of nano-size precipitation and mechanical properties in a high strength-ductility low alloy steel through intercritical treatment. Mater Sci Eng A 2017;705:89–97. https://doi.org/10.1016/j.msea.2017.08.061.

[69] Zhou ZR, Nakazawa K, Zhu MH, Maruyama N, Kapsa P, Vincent L. Progress in fretting maps. Tribol Int 2006;39:1068–73. https://doi.org/10.1016/j.triboint.2006.02.001.

[70] Zhou ZR, Vincent L. Mixed fretting regime. Wear 1995;181–183:531–6. https://doi.org/10.1016/0043-1648(95)90168-X.

[71] Zhou ZR, Vincent L. Effect of external loading on wear maps of aluminium alloys. Wear 1993;162–164:619–23. https://doi.org/10.1016/0043-1648(93)90552-W.

[72] Zhu MH, Zhou ZR. On the mechanisms of various fretting wear modes. Tribol Int 2011;44:1378–88. https://doi.org/10.1016/j.triboint.2011.02.010.

[73] Fouvry S, Kapsa P, Vincent L. Quantification of fretting damage. Wear 1996;200:186–205. https://doi.org/10.1016/S0043-1648(96)07306-1.

[74] Fouvry S, Kapsa P, Vincent L. Analysis of sliding behaviour for fretting loadings: determination of transition criteria. Wear 1995;185:35–46. https://doi.org/10.1016/0043-1648(94)06582-9.

[75] Mindlin RD. Compliance of elastic bodies in contact. J Appl Mech 2021;16:259–68. https://doi.org/10.1115/1.4009973.

[76] Zhu H, Xiong Z, Mao J, Cheng X. Low-cost secondary hardening steel under double ageing: Dual-precipitation control, austenite modification and strength-toughness improvement. Mater Sci Eng A 2025;931:148159. https://doi.org/10.1016/j.msea.2025.148159.

[77] Ding F, Guo Q, Hu B, Xu Y, Lai W, Zhang C, et al. Influences of Cu alloying on precipitation, austenitic reversion and mechanical properties of NiAl-strengthened medium-Mn steels. Acta Mater 2025;284:120623. https://doi.org/10.1016/j.actamat.2024.120623.

[78] Sun H, Li D, Diao Y, He Y, Yan L, Pang X, et al. Nanoscale Cu particle evolution and its impact on the mechanical properties and strengthening mechanism in precipitation-hardening stainless steel. Mater Char 2022;188:111885. https://doi.org/10.1016/j.matchar.2022.111885.

[79] Murayama M, Hono K, Katayama Y. Microstructural evolution in a 17-4 PH stainless steel after aging at 400 °C. Metall Mater Trans A 1999;30:345–53. https://doi.org/10.1007/s11661-999-0323-2.

[80] Mahadevan S, Manojkumar R, Jayakumar T, Das CR, Rao BPC. Precipitation-Induced changes in microstrain and its relation with Hardness and tempering parameter in 17-4 PH stainless steel. Metall Mater Trans A 2016;47:3109–18. https://doi.org/10.1007/s11661-016-3440-8.

[81] Wang Z, Fang X, Li H, Liu W. Atom probe tomographic characterization of nanoscale Cu-Rich precipitates in 17-4 precipitate hardened stainless steel tempered at different temperatures. Microsc Microanal 2017;23:340–9. https://doi.org/10.1017/S1431927616012629.

[82] Xiong Z, Timokhina I, Pereloma E. Clustering, nano-scale precipitation and strengthening of steels. Prog Mater Sci 2021;118:100764. https://doi.org/10.1016/j.pmatsci.2020.100764.

[83] Xu XJ, Xu W, Ederveen FH, van der Zwaag S. Design of low hardness abrasion resistant steels. Wear 2013;301:89–93. https://doi.org/10.1016/j.wear.2013.01.002.

[84] Torres H, Varga M, Widder F, Cihak-Bayr U, Viskovic O, Rodríguez Ripoll M. Experimental simulation of high temperature sliding contact of hot rolled steel. Tribol Int 2016;93:745–54. https://doi.org/10.1016/j.triboint.2015.01.007.

[85] Li XX, Zhou Y, Li YX, Ji XL, Wang SQ. Dry sliding wear characteristics of Ti-6.5Al-3.5Mo-1.5Zr-0.3Si alloy at various sliding speeds. Metall Mater Trans A 2015;46:4360–8. https://doi.org/10.1007/s11661-015-3019-9.